**Correspondence to:**
J. H. Fairweather,
john.fairweather@postgrad.curtin.edu.au

**Author Contributions:**
**Conceptualization:** A. Lagain
**Data curation:** J. H. Fairweather, K. Servis
**Formal analysis:** J. H. Fairweather, K. Servis
**Funding acquisition:** G. K. Benedix
**Investigation:** J. H. Fairweather, A. Lagain

# Lunar Surface Model Age Derivation: Comparisons Between Automatic and Human Crater Counting Using LRO-NAC and Kaguya TC Images

**J. H. Fairweather[1]**, **A. Lagain[1]**, **K. Servis[1,2]**, and **G. K. Benedix[1,3,4]**

[1]Space Science and Technology Centre, School of Earth and Planetary Sciences, Curtin University, Perth, WA, Australia, [2]CSIRO, Pawsey Supercomputing Centre, Kensington, WA, Australia, [3]Department of Earth and Planetary Sciences, Western Australia Museum, Welshpool, WA, Australia, [4]Planetary Science Institute, Tucson, AZ, USA

**Abstract** Dating young lunar surfaces, such as impact ejecta blankets and terrains associated with recent volcanic activities, provides critical information on the recent events that shaped the surface of the Moon. Model age derivation of young or small areas using a crater chronology is typically achieved through manual counting, which requires a lot of small impact craters to be tediously mapped. In this study, we present the use of a Crater Detection Algorithm (CDA) to extract crater populations on Lunar Reconnaissance Orbiter— Narrow Angle Camera (LRO-NAC) and Kaguya Terrain Camera images. We applied our algorithm to images covering the ejecta blankets of four Copernican impact craters and across four young mare terrains, where manually derived model ages were already published. Across the eight areas, 10 model ages were derived. We assessed the reproducibility of our model using two populations for each site: (a) an unprocessed population and (b) a population adjusted to remove contaminations of secondary and buried craters. The results showed that unprocessed detections led to overestimating crater densities by 12%–48%, but "adjusted" populations produced consistent results within <20% of published values in 80% of cases. Regarding the discrepancies observed, we found no significant error in our detections that could explain the differences with crater densities manually measured. With careful processing, we conclude that a CDA can be used to determine model ages and crater densities for the Moon. We also emphasize that automated crater datasets need to be processed, interpreted and used carefully, in unity with geologic reasoning. The presented approach can offer a consistent and reproducible way to derive model ages.

**Plain Language Summary** Studying young lunar surfaces, such as impacted areas or volcanic activity, helps us understand recent events that have shaped the Moon's surface. Determining the model age of these areas generally involves manually counting small craters, which is time-consuming and variable. This study presents a machine-learning approach to detect craters on images acquired by the Lunar Reconnaissance Orbiter-Narrow Angle Camera and the Kaguya Terrain Camera. Four impact craters and four young mare terrains were analyzed, where model ages had already been determined manually. When comparing our automatic counts to the manual counts, we observed that our results became more consistent with the published surface ages when we excluded secondary or buried craters from our crater populations. We also outline that automatic crater detection methods can be used to determine the age of lunar surfaces in a reliable and consistent manner when used correctly.

## 1. Introduction

The surface of the Moon has recorded the impact history of the inner solar system for the last ∼4 billion years (Öpik, 1960; Shoemaker & Hackman, 1962). The counts of impact craters that have accumulated on geological units, which have been radiometrically dated thanks to sample return missions, have allowed researchers to establish a lunar chronology system that can link the measured crater density with a model age for any mapped unit (e.g., Neukum et al., 2001; Shoemaker & Hackman, 1962). When applied to the ejecta blanket, or the floor, of large impact craters, the crater counts allow one to estimate the age of the impact event (Hiesinger et al., 2012; Kirchoff et al., 2021; Lagain, Benedix, et al., 2021; Lagain, Servis, et al., 2021; Lagain et al., 2020). Copernican-aged craters (<1.1 Ga) are interpreted as the most recent impacts across Moon's surface. These craters are characterized by their bright ejecta and fresh morphology, making them ideal for mapping (Dundas & McEwen, 2007; Wilhelms, 1987). However, many Copernican craters smaller than ∼20 km in diameter have

**Methodology:** J. H. Fairweather, A. Lagain, K. Servis
**Project Administration:** A. Lagain
**Software:** K. Servis
**Supervision:** A. Lagain, K. Servis, G. K. Benedix
**Writing – original draft:** J. H. Fairweather, A. Lagain, G. K. Benedix
**Writing – review & editing:** A. Lagain, G. K. Benedix

few, or no, associated ages, which impedes the investigation of smaller-scale events in recent lunar time. Equally, small and/or recent (<3 Ga) geological units associated with later volcanic episodes are also sporadically dated. This has been due to time limitations in geological mapping on high-resolution image datasets and crater identification (i.e., mapping all craters <1 km in diameter). Therefore, a method for quickly and systematically analyzing Copernican craters of all sizes, and more generally, young geological units is needed.

The introduction of Machine Learning (ML) techniques, such as Convolutional Neural Networks (CNNs), can help in overcoming some of the limitations. Crater Detection Algorithms (CDA) have already been developed and optimized for use on planetary images to detect impact structures quickly and accurately (e.g., Benedix et al., 2020; DeLatte et al., 2019; Lagain, Benedix, et al., 2021; Lagain, Bouley, et al., 2022; Lagain, Kreslavsky, et al., 2022; Lagain, Servis, et al., 2021; Fairweather et al., 2022). If a CNN's performance is similar to human-level error (Robbins et al., 2014; Wang et al., 2020) and used with caution (e.g., removal of secondary crater clusters and avoidance of overprinted craters (Fassett, 2016; Fassett & Thomson, 2014; Xu et al., 2022)), automatically detected crater datasets can be used to derive meaningful Crater Size-Frequency Distributions (CSFD) and model ages (Benedix et al., 2020; Lagain, Bouley, et al., 2022). With further use and analysis of the crater detections, it is possible to derive acceptable surface ages for hundreds of sites (Lagain, Bouley, et al., 2022). Although there have been many successful attempts to create CDAs to address the lunar crater populations (e.g., Ali-Dib et al., 2020; Cadogan, 2020; Salamunićcar et al., 2014; Sawabe et al., 2006; Yang et al., 2020), to our knowledge, no study has systematically used automatic crater counts to derive model ages and determined if they are comparable with manual methods. The ML approach is particularly relevant for investigating younger surfaces, such as those found around the Chang'E-5 (CE-5) landing site (LS) and Copernican crater ejecta.

To quantify the viability and accuracy of using a CDA to analyze Copernican impacts and relatively recent lunar surfaces, we compare a set of published model ages with the model ages derived using our CDA. The automatically detected craters were obtained from the global Kaguya Terrain Camera (TC) images (∼7 m/px resolution) (Haruyama et al., 2008) and the Lunar Reconnaissance Orbiter - Narrow Angle Camera (LRO-NAC, ∼0.25–2 m/px resolution) (Robinson et al., 2010) image datasets. Specifically, we focused on model ages and cratering densities reported for North Ray, Tycho, Copernicus (see Hiesinger et al., 2012) and Lalande craters (see Xu et al., 2022); as well as two mare areas in the vicinity of the Chang'E-5 mission LS (areas #05 and #21 in Giguere et al., 2022); and two regional mare units, Oceanus Procellarum unit P60 (see Hiesinger, 2003), and Imbrium unit I30 (see Hiesinger et al., 2000). These sites are well-known and commonly investigated, therefore they serve as acceptable points of comparison.

## 2. Data and Methodology

The following sections describe the locations of the crater count areas we selected. We describe the two CDA detection models optimized for NAC (Fairweather et al., 2022) and the Kaguya TC image data set (this study). We also detail the process for deriving the model ages and removing the potential contaminations of secondary and overprinted craters (referred to as "pre-existing" craters within this study).

### 2.1. Surface Model Age of the Crater Counts Areas

Each count area was chosen based on four main criteria: (a) the availability of high-resolution images (either in NAC, Kaguya TC, or both), (b) relatively young published model ages (either Copernican or Eratosthenian, i.e., <3.2 Ga), (c) the ability to compare against prior manual crater directly counts within the literature, and (d) a spread across lunar terrains among the selected study areas. Four Copernican impact craters (North Ray, Lalande, Tycho, Copernicus) and four Eratosthenian mare surfaces (CE-5 #05 and #21, P60, I30) were selected based on these criteria (Figure 1 and Table 1). We note that in the case of Lalande crater, two crater densities are reported from the same count area: one related to the crater emplacement and another to the terrain underlying the ejecta blanket. In total, 10 crater density measurements (Table 1) across seven areas were investigated (Figure 1).

### 2.1.1. The Copernican Craters

The craters investigated within this study are all younger than 1.1 Ga and lie within the Copernican chronology system. Each of the craters can be defined by their bright crater ray systems, visible ejecta blankets, and clean crater rims (Dundas & McEwen, 2007; Wilhelms, 1987). The four chosen craters are (from smallest to largest):
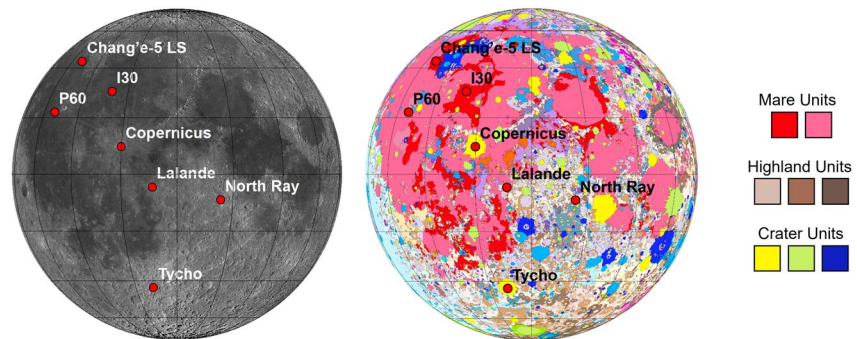
**Figure 1.** Left: Locations of the chosen crater count areas investigated in this study. The two areas around the Chang'e-5 landing site are symbolized by one dot on the map. The background is a stereographic projection of the LRO-WAC mosaic (Speyerer et al., 2011). Right: The unified geologic map of the near side of the Moon in a stereographic projection, with a simplified geological unit key (For the whole map, see Fortezzo et al., 2020).

North Ray, Lalande, Tycho, and Copernicus. These impacts are spread across the nearside of the Moon and are superimposed across a range of lunar lithologies (Figure 1, Table 1). The smallest investigated crater, North Ray ($D \sim 1$ km), was visited and sampled during the Apollo 16 mission, where the exposure age of some material collected nearby allowed to provide a calibration point for the lunar chronology model (Table 1). Lalande crater (D $\sim$ 24 km) was dated and investigated in depth by Xu et al. (2022), their findings are reported in later sections. Finally, the two most prominent lunar impacts, Tycho crater (D $\sim$ 85 km) and Copernicus crater (D $\sim$ 95 km). These craters have been thoroughly mapped and investigated over the years (e.g., Dundas & McEwen, 2007; Mazrouei et al., 2019; Pozzobon et al., 2020; Wilhelms, 1987). Their formation has been associated with lunar material collected from Apollo 17 and Apollo 12 missions, respectively (Table 1). However, we note that a 1:1 comparison with the radiometric age of some of the Apollo 17 samples and the model age obtained from crater counts performed on Tycho's ejecta has been recently questioned by the community and ruled out in recent lunar chronology recalibrations (e.g., Robbins, 2014; Xie & Xiao, 2023). Indeed, Schmitt et al. (2017) argued that the avalanche deposits on which crater counts were performed and originally interpreted as being triggered by Tycho's formation, would instead be associated with the Lee-Lincoln fault. Therefore, we will not compare the exposure age of the light mantle avalanche debris within Taurus-Littrow and the crater counts on Tycho's ejecta. These four craters have been investigated using crater count methods in the literature, especially Tycho and Copernicus (see, Mazrouei et al., 2019; Xiao & Strom, 2012; Xiao & Werner, 2015; Terada et al., 2020). Therefore, they serve as good candidates to analyze and compare our CDA model results in order to investigate differences and

**Table 1**
*Information on Each Count Area Location Investigated Within This Study*

| Type | Location/Count area | | Diameter/Area | | Latitude | Longitude | Terrain | Radiometric age |
|---|---|---|---|---|---|---|---|---|
| Copernican Crater | North Ray | | 1 km | | 8.82°S | 15.48°E | Nearside Descartes Highlands | 50.3 ± 0.8 Ma Drozd et al. (1974) |
| | Lalande | | 24 km | | 4.4°S | 8.6°W | Eastern Mare Insularum | / |
| | *Tycho | NAC | 85 km | 1.65 km² | 43.31°S | 11.36°W | Nearside southern Highlands | 110 ± 4 Ma Drozd et al. (1977) |
| | | WAC | | 6,710 km² | | | | |
| | *Copernicus | | 95 km | | 9.62°N | 20.08°W | Eastern Oceanus Procellarum | 800 ± 15 Ma Bogard et al. (1992) |
| Eratosthenian Mare | Chang'E-5 | #05 | 48 km² | | 43.05°N | 51.91°W | North-Eastern Oceanus Procellarum | 2030 ± 4 Ma Li et al. (2021) |
| | | #21 | 272 km² | | | | | |
| | Mare Unit P60 | | 1,429 km² | | 22.0°N | 53.0°W | Central Eastern Oceanus Procellarum | / |
| | Mare Unit I30 | | 3,108 km² | | 30.0°N | 27.0°W | Western Mare Imbrium | / |

*Note.* Coordinates are in decimal degrees. *Denotes the locations were indirectly sampled.

viability in dating such impacts. Reported age results from the chosen crater studies (i.e., Hiesinger et al., 2012; Xu et al., 2022) are summarized in Table 2.

### 2.1.2. The Mare Units

The analyzed mare units cluster in the north-western hemisphere of the Moon's near side (Figure 1). Two sites associated with the Chang'E-5 sample return mission (Che et al., 2021) were chosen due to a significant variation in the reported cratering densities (see Giguere et al., 2022). They are both located within Oceanus Procellarum, a mare unit of great interest as it is estimated to be one of the youngest mare flows on the Moon's surface (Figure 1) and has had extensive investigation within recently published studies (e.g., Giguere et al., 2022; Jia et al., 2020; Qian et al., 2021; Wu et al., 2018) (Table 2). The first area, mare unit (#21), is located in the immediate vicinity of the Chang'E-5 lunar lander (Table 1). Count area #05 is ~15 km east of area #21. The two remaining units are also young mare flows; Oceanus Procellarum mare unit P60 and Imbrium mare unit I30 (Figure 1, Table 1). These areas were defined and dated with crater counts by Hiesinger et al. (2000, 2011), and Hiesinger (2003) (Table 2). Unlike the Change-5 LS, these mare units do not have any known associated radiometric ages assigned to their formation (Table 1).

### 2.2. The Image Data Sets

To analyze each of the crater count areas, we used images from two lunar image datasets. The first was the LRO-NAC image data set, which has a spatial resolution ranging between 0.25 and 2 m/px (Robinson et al., 2010), allowing consistent mapping of craters down to ~20 m in diameter (Robbins et al., 2014; Wang et al., 2019). For the small North Ray and Tycho (NAC TE) count areas (Table 2), we used NAC image pairs M129187331R/L and M104570590R/L (note: these are the same NAC images used by Hiesinger et al. (2012) in their study of the same locations). The NAC images were downloaded through the online LROC PDS portal (https://wms.lroc.asu.edu/lroc/search) and were processed through the USGS Integrated Software for Imagers and Spectrometers (ISIS).

The second image data set was the global mosaicked Kaguya TC images (Haruyama et al., 2008; Isbell et al., 2014). Across the cited literature we analyzed within this study, the count areas for Tycho (WAC TE), Copernicus, and Lalande craters, Chang'E-5 (#05, #21), P60 and I30 units were derived from crater counts performed on WAC, Lunar Orbiter IV, and Kaguya TC camera images (Table 2). Among these areas, the smallest crater diameter used to derive a model age was 100 m, measured on Kaguya TC images by Xu et al. (2022). The Kaguya TC data set provides an excellent bridge to the resolution gaps between Lunar Orbiter IV/LRO-WAC and LRO-NAC datasets, with a near-global coverage at ~7.4 m/px in resolution (Haruyama et al., 2008). Therefore, we used the Kaguya TC images in place of the LRO-WAC and Lunar Orbiter IV images for Tycho (area WAC TE), Copernicus, P60 and I30 count areas. Two mosaicked versions of the Kaguya TC data set were used: a morning version (with early or right-to-left low-angle solar illumination) and an evening version (with late or left-to-right solar illumination). Both datasets are released as 3° by 3° image tiles (see, Isbell et al., 2014; Kaguya Data Archive, https://darts.isas.jaxa.jp/planet/pdap/selene/). The Kaguya TC image tile ID list for each count area is reported in Table S1 in Supporting Information S1.

### 2.3. The Crater Detection Algorithm

Our CDA is a CNN image-based object detection algorithm which has been developed to identify impact craters on multiple scales across both Martian (Benedix et al., 2020; Lagain, Benedix, et al., 2021; Lagain, Servis, et al., 2021) and lunar (Fairweather et al., 2022) images. Specifically, the prior CNN models use the Ultralytics implementation of YOLOv3 (You Only Look Once version 3, Redmon et al., 2016).

Within this study, we have utilized two crater detection CNN models. The first was trained for detection across LRO-NAC images with intermediate lighting conditions (incidence angle ~50°–70°) (Fairweather et al., 2022). This detection model has good detection accuracy, with an average Recall of 0.93 (crater detection rate), a Precision of 0.66, and an F1 score of 0.77 for craters down to ~20 m in size (Fairweather et al., 2022). When evaluating against craters >100 m in diameter, we obtained a Recall of 0.99 for fresh and moderately degraded craters, which decreases to 0.85 for very-degraded craters (see Fairweather et al., 2022). The NAC model was applied on images M129187331R/L and M104570590R/L (in a stereographic map projection), where we determined the CSFDs for North Ray and Tycho ejecta, respectively. An example of raw CDA detections on NAC images is shown in

**Table 2**
*Published Information of Each Location, Image Data, Unit ID, Size of Count Area, $N_{cum}(1)$ [per $km^2$], and Model Age (With Errors)*

| Location | Study | Image Data | Count Area | Area ($km^2$) | Number of Craters | Fit Range | $N_{cum}(1)$ | Model age (Ma) | Error (Ma) |
|---|---|---|---|---|---|---|---|---|---|
| North Ray | Hiesinger et al. (2012) | NAC | NR1-4 | 2.12 | 4177[a] | 20–100 m | 3.94E−05 | 47 | 4 / −4 |
| Lalande | Xu et al. (2022) | Kaguya TC | Ejecta blanket on Mare | 1,780 | 1540[b] | 100–170 m | 3.35E−04 | 400 | 9 / −9 |
| | | | | | 12[b] | >1.2 km | 1.81E−02 | 3800 | 40 / −60 |
| Tycho | Hiesinger et al. (2012) | NAC | NAC TE1-4 | 1.65 | 12,698[a] | 20–100 m | 7.12E−05 | 85 | 15 / −18 |
| | | WAC | WAC TE | 6,710 | 266[a] | 150 m–1 km | 1.04E−04 | 124 | 12 / −12 |
| Copernicus | Hiesinger et al. (2012) | WAC | WAC CE1-3 | 2,630 | 534[a] | 200 m–1 km | 6.53E−04 | 779 | 110 / −120 |
| Chang'E-5 | Giguerre et al. (2022) | NAC | #21 | 48 | 49[b] | 200–600 m | 2.61E−03 | 3030 | 200 / −300 |
| | | NAC | #05 | 272 | 100[b] | 200 m–1 km | 2.15E−03 | 2560 | 200 / −300 |
| Oceanus Procellarum P60 | Hiesinger (2003) | Lunar Orbiter IV | P60 | 1,429 | / | >400 m | 1.01E−03 | 1200 | 320 / −320 |
| Mare Imbrium I30 | Hiesinger et al. (2000) | Lunar Orbiter IV | I30 | 3,108 | / | >400 m | 1.68E−03 | 2010 | 140 / −140 |

*Note.* The published $N(1) = 1.86E−02\ km^{−2}$ value reported in Xu et al. (2022) for Lalande's impacted mare terrain using 12 craters >1.2 km was incorrect for the reported model age. Therefore we have reported the corrected value of $N(1) = 1.81E−02\ km^{−2}$. Model ages for North Ray, Lalande, Tycho, Copernicus and Chang'E-5 areas were calculated from the fit of the cumulative CSFD to the Neukum et al. (2001) production function. The model ages for Oceanus Procellarum unit P60 and Mare Imbrium unit I30 were calculated from the fit of cumulative CSFD to the Neukum (1984) production function.

[a]Number of craters counted within the count area. [b]Number of craters within the fit range.
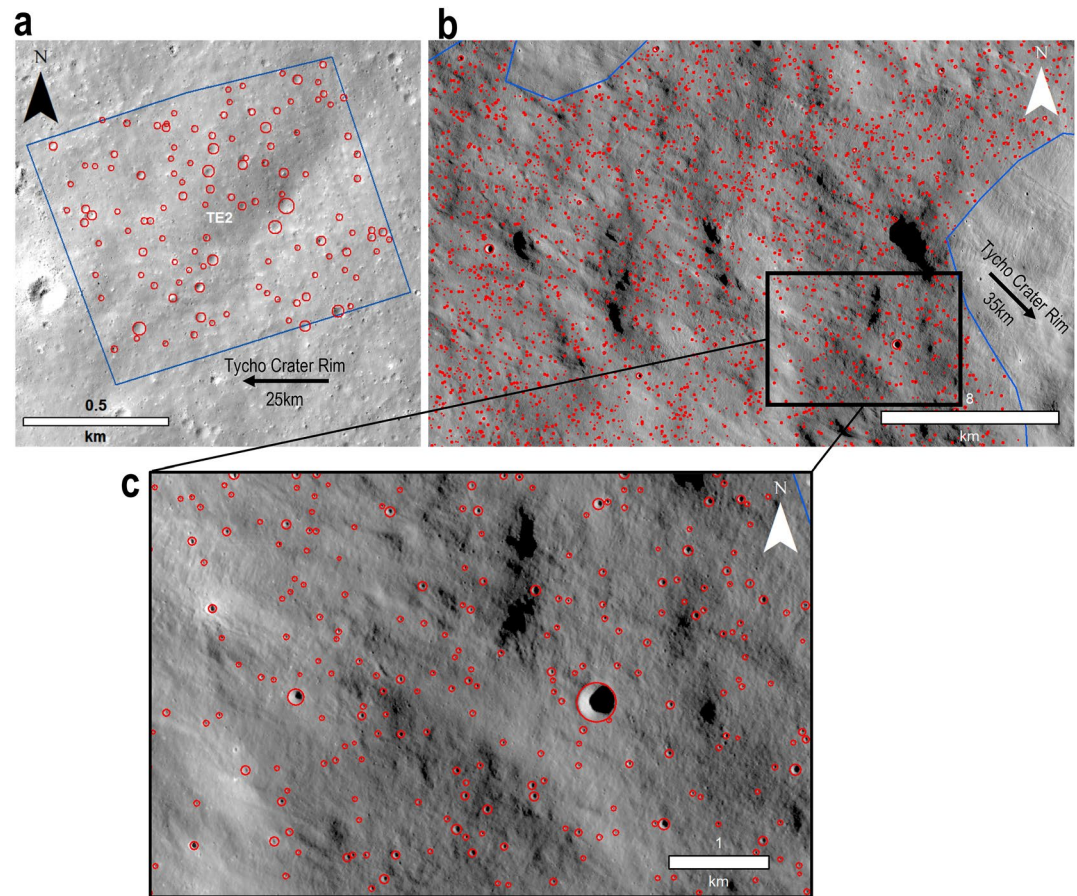
**Figure 2.** Examples of raw crater detections over Tycho's ejecta. (a) Sample of 115 craters (10 m < D < 40 m) detected over Hiesinger et al. (2012)'s TE2 region on NAC image M104570590 L; (b) Sample of 3176 craters (38 m < D < 396 m) detected over Hiesinger et al. (2012)'s north-eastern WAC TE region on Kaguya image tile TCO_MAPm04_S39E345S42E348SC (see Figure 4 for crater context); (c) Zoomed in excerpt of the [b] Kaguya sample showing of 396 craters (38 m < D < 396 m). All crater detections in Data Set S2. Note, the missing crater detections across these images are below the 10-pixel reliability threshold for the CDA—these small craters are shown here but were not used to our derive model age.

Figure 2a. While using the NAC detection model, crater diameters were overestimated by ~15% (see Fairweather et al., 2022). Therefore, following the findings from Fairweather et al. (2022), the diameter sizes for the detections on the NAC images used within this study were corrected by a factor of −0.15 to display the model ages more accurately (see Figure S3 in Supporting Information S1 for the before and after 15% diameter correction).

To detect impact craters across Kaguya TC mosaics, our algorithm was updated with the Ultralytics' YOLOv5 (Jocher, 2022; https://github.com/ultralytics/yolov5), and newly trained on both morning and evening Kaguya versions (refer to the Text S1 in Supporting Information S1 for a description of the model retraining). The training data set comprised 55,348 craters over 485 image tiles, with a 3:1 learning-validation split. The metrics obtained at the end of the training session were 0.8 for the Recall and 0.8 for the Precision, leading to an F1 score of 0.8 (Figure S1 in Supporting Information S1). To further evaluate the performance of our model as recommended by Fairweather et al. (2022), we compiled two manual crater test datasets for both morning and evening Kaguya TC tiles. Each data set has two subsets, each over the same mare and highland terrains (refer to the Text S2 in Supporting Information S1 for a full description of the evaluation results). This resulted in a Recall of 0.98, a Precision of 0.94 and an F1 score of 0.96 for craters >100 m in diameter (see Table S2 in Supporting Information S1 and Data Set S1). The reader is referred to Fairweather et al. (2022), Section 3.1 for further explanations of the metrics differences obtained between the validation datasets and the test datasets. Furthermore, the new model removed the systematic size overestimation (Figure S2 in Supporting Information S1) that the prior YOLOv3 NAC model displayed (see, Fairweather et al., 2022).
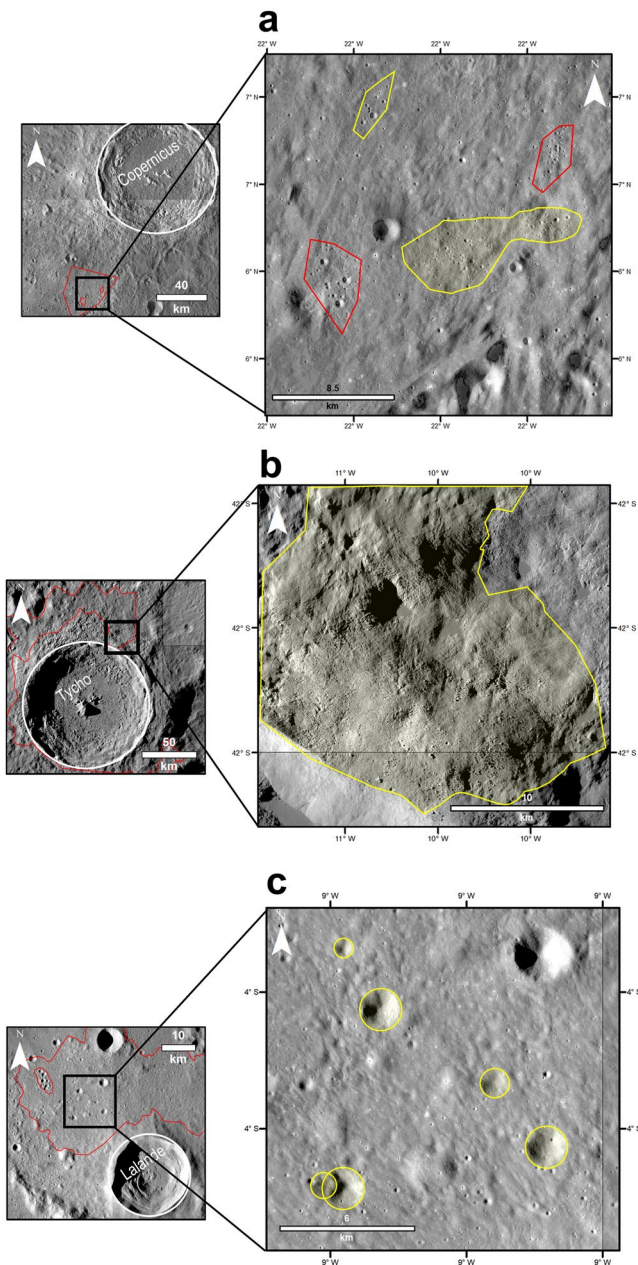
**Figure 3.** Examples of the features that were removed from the crater count datasets. (a) Secondary crater clusters within the Copernicus count area, red polygons denote the areas defined and identified by Hiesinger et al. (2012), yellow polygons denote an additional cluster identified and removed within this study; (b) Rocky regions with poor lighting conditions within the Tycho count area, red polygons denote the count area defined by Hiesinger et al. (2012), yellow polygon denotes an unsuitable area for crater identification; and (c) "Pre-existing" craters (yellow circles) across the Lalande count area, red polygon denotes the count area defined by Xu et al. (2022). Kaguya image tile IDs for each site are in Table S1 in Supporting Information S1. Raw and adjusted count areas for all sites are available in Data Set S2.

The updated Kaguya CDA model was applied to both Kaguya TC morning and evening mosaic tiles covering Tycho, Copernicus, and Lalande ejecta count areas, as well as the Chang'E-5 areas, P60, and I30 units (all in stereographic map projections). The model was applied to the images listed in Table S1 in Supporting Information S1 using the Pawsey Supercomputing Center's supercomputer clusters (see, Pawsey, 2023 and Fairweather et al., 2022). Due to the difference in illumination angles and data quality between the two versions of the Kaguya TC mosaics (Isbell et al., 2014), only the tile datasets with the highest number of detections were kept. Some examples of raw CDA detections across Kaguya TC images are shown on Figures 2b and 2c.

### 2.4. Count Areas and Crater Data Selection

Our automatic approach does not discriminate secondary craters (Figure 3a) and "pre-existing" craters (buried or overlapped by ejecta blankets, Figure 3b) from primary craters. Therefore, we adapted a crater selection method to overcome these limitations and extract a crater population that best represents the formation age of the unit. Before applying the method, the smallest possible crater that can be accurately mapped and reliably identified across planetary images must be $\geq 10$ pixels in diameter (Robbins et al., 2014; Wang et al., 2020). For this study, this translates to craters ~20 and ~70 m in diameter for LRO-NAC images and Kaguya TC images, respectively. Therefore, when using a CDA, we cannot reliably derive ages from craters smaller than the stated thresholds. Also, deriving model ages from recent impact events requires careful counting of small craters superimposed on the ejecta blanket and removing areas dominated by secondary craters (Lagain, Servis, et al., 2021; Lagain et al., 2020; Xu et al., 2022; Zanetti et al., 2017). Here we describe a suitable method for discarding/identifying such craters from within the determined count areas.

First, we split our model age derivation analysis in two; this is aimed at keeping the analysis as transparent as possible. The first set of analyses compared our "raw" CSFDs, derived from the "raw" CDA craters within the exact same published counting areas (Table 2), to the published values. This analysis reflects a fully automatic approach, using every crater detected by our algorithm. The second set of comparisons compared CSFDs made from an "adjusted" CDA data set across updated counting crater count areas and crater counts with contaminates removed. The process for generating the adjusted crater datasets is described below.

Prominent secondary crater clusters and areas unsuitable for crater identification (i.e., Figures 3a and 3b) were manually identified and subsequently removed across the analyzed sites. Secondary craters lead to an overestimation of the cratering densities, and topographically unsuitable terrains do not retain the needed small craters (Craddock & Howard, 2000), thus leading to erroneous model ages. Some of the cited literature did not clearly outline their method for identifying and removing such features. Xu et al. (2022) identified and removed a secondary crater cluster from their counting area on Lalande's ejecta. Additionally, Giguere et al. (2022) also described and removed a secondary crater cluster area from the Chang'E-5 LS area #21. However, except for two areas corresponding to secondary clusters within the WAC CE2 area, Hiesinger et al. (2000, 2011, 2012) and Hiesinger (2003) did not report any crater clusters within their mapped areas for North Ray, Tycho, P60, and I30. It is reasonable to think that obvious secondary craters were not included in their crater count datasets. Therefore, we adjusted the count areas outlined by Hiesinger et al. (2000, 2011, 2012), and
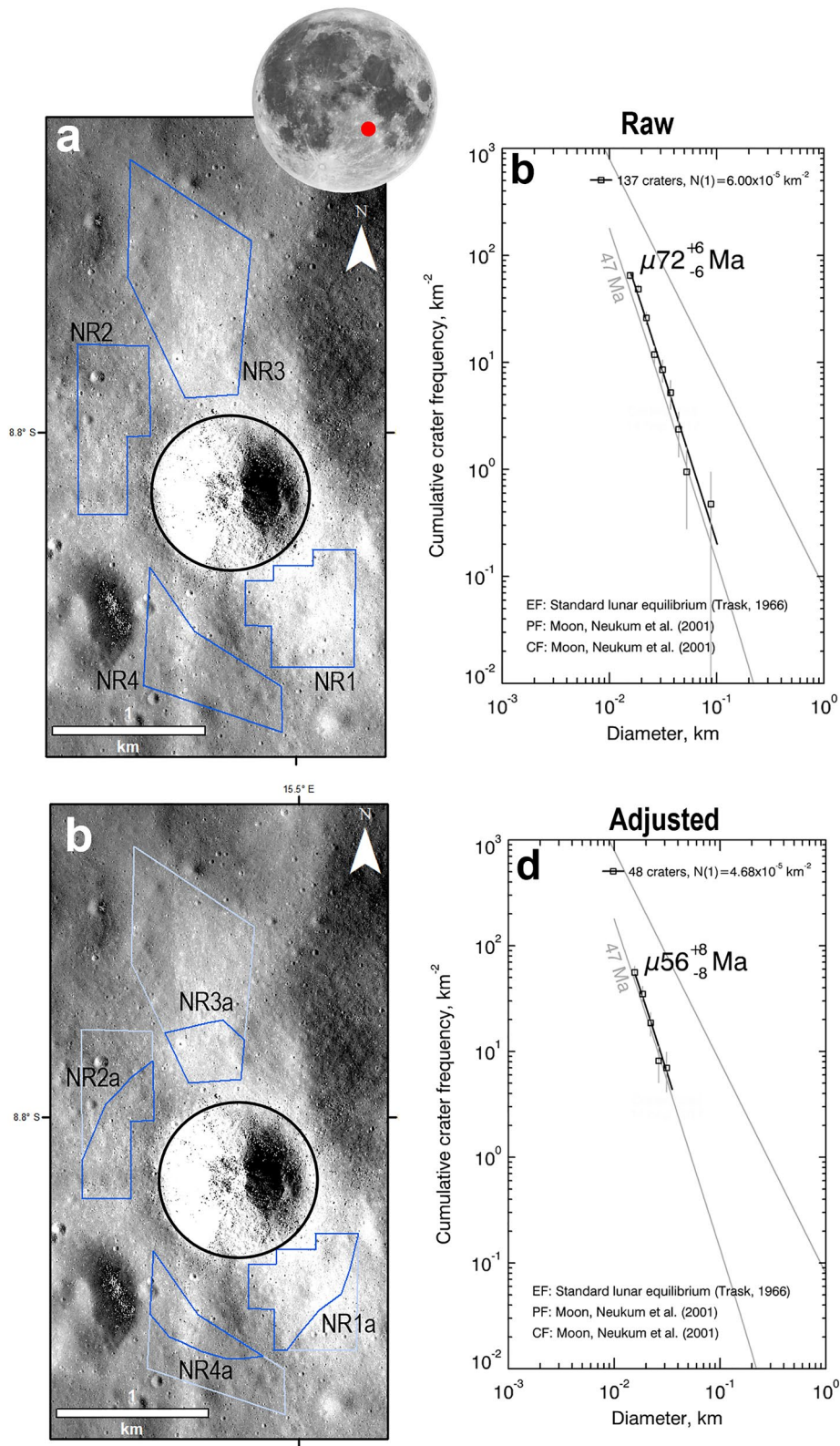
**Figure 4.**

Hiesinger ([2003](#)) by discarding areas displaying obvious clusters and inadequate morphologies (such as shown in Figure [3b](#)). Moreover, Hiesinger et al. ([2012](#))'s NAC count area TE3 was excluded from our analysis due to lighting challenges and count area topography difficulties (see Figure S5 in Supporting Information [S1](#)). Therefore, for the comparative analysis, we only used count areas TE1, 2, and 4. Additionally, Hiesinger et al. ([2000](#), [2011](#)), and Hiesinger ([2003](#)) do not specifically report or show their crater size ranges used to fit the CSFD isochrons for units P60 and I30. However, the resolutions of the images used (~60–150 m/px, Hiesinger et al., [2011](#)) imply that craters larger than ~400 m were used, thus constituting the cut-off size we applied to the detections obtained from the Kaguya TC images over these two areas.

The identification and removal of craters overprinted by impact ejecta blankets (i.e., "pre-existing" craters, Figure [3c](#)) were performed by implementing a semi-automatic technique outlined by Fassett and Thomson ([2014](#)) and used by Xu et al. ([2022](#)). The technique estimates if a "pre-existing" crater should be seen/detected after an impact event, accounting for its distance from the impact crater and the radial ejecta blanket thickness. This process was replicated and adapted from Xu et al. ([2022](#))'s dating technique for Lalande crater. Though, our method differs slightly: where Xu et al. ([2022](#)) used one ejecta thickness model (i.e., Pike ([1974](#))'s equation [Equation [3](#)]), we introduced two additional models from Sharpton ([2014](#)) for simple (2.2–17 km) [Equation [1](#)] and complex craters (17–45 km) [Equation [2](#)], defined as follow:

$$T = 0.014 \times R^{1.01} \times \left(\frac{r}{R}\right)^{-3} (2.2\,\text{km} < D < 17\,\text{km}) \tag{1}$$

$$T = 3.95 \times R^{0.399} \times \left(\frac{r}{R}\right)^{-3} (17\,\text{km} < D < 45\,\text{km}) \tag{2}$$

$$T = 0.033 \times R \times \left(\frac{r}{R}\right)^{-3} (D > 45\,\text{km}) \tag{3}$$

Where $T$ is the ejecta thickness at a distance of $r$ from the impact crater center, and $R$ is the transient radius of the impact crater, calculated using $R \times 0.85$ (Baldwin, [1964](#); Hildebrand et al., [1998](#); Melosh, [1989](#); Pike, [1974](#)).

However, this set of equations estimates the ejecta thickness deposited on a planar surface. Previous studies (e.g., Xie & Zhu, [2016](#); Xu & Xie, [2020](#)) have shown that the thickness of ejecta filling up "pre-existing" craters is approximately ~2.9 times thicker than that deposited on flat surfaces due to the concave-upward shape of the crater cavity. Therefore, following Xu and Xie ([2020](#))'s method, Equations [1](#)–[3](#) were modified to account for the increased thickness of ejecta material within "pre-existing" craters by applying a factor of 2.9 to the calculated ejecta thickness ($T$). Additionally, using the average depth-to-diameter ratios (0.12 for craters 40m < D < 100 m, 0.15 for 100m < D < 400 m, and 0.2 for 400m < D < 5 km) for simple craters ranging between 40 m and 5 km inferred by Stopar et al. ([2017](#)), we can assume the maximum depth of all detected craters and compare it to the ejecta thickness at each crater. Craters with a depth shallower than the expected ejecta thickness were flagged. Detected craters found to be overlain by the ejecta blanket, as well as being of secondary origin, were checked and removed from the crater data set. The count area polygons were also adjusted based on these findings, where areas overwhelmingly dominated in secondary craters, "pre-existing" craters, and areas unsuitable for crater identification (Figure [3](#)) were removed. These changes combine to form the adjusted CDA crater datasets used to produce the adjusted CFSDs. All crater detections are available in the Data Set [S2](#).

## 3. Results

The following two sub-sections present the results from the comparative crater count analysis that was undertaken to show the application of the CDA in determining the ages of young/small geological units. We present the 'raw' and 'adjusted' CSFDs inferred from our CDA crater data sets for each crater count area. All CSFD isochrons were fitted using the same crater fit ranges as the published studies (see Table [2](#)). The crater size ranges we used to derive the model ages were not in equilibrium (defined by the Trask ([1966](#)) stand lunar equilibrium function). All CSFDs were made using CraterStats II (Michael & Neukum, [2010](#)). We kept the chronology systems for each

**Figure 4.** (a) Hiesinger et al. ([2012](#))'s North Ray crater count areas NR1-4 (blue polygons, 2.12 km²) on NAC image pair M129187331R/L; (b) CSFD and model age for areas NR1-NR4 using 137 craters between 17 and 100 m in diameter detected by the CDA; (c) this study's adjusted count areas NR1a-NR4a (blue polygons, 0.86 km²) for North Ray Crater on NAC image pair M129187331R/L; (d) adjusted CSFD and absolute model age for areas NR1a-NR4a using 48 automatically detected craters between 17 and 40 m in diameter. The gray 47 Ma isochron plotted on panels (b and d) corresponds to that reported by Hiesinger et al. ([2012](#)). The crater images are presented in a stereographic map projection, with the count area locations (see Table [1](#)) as the projection center point.
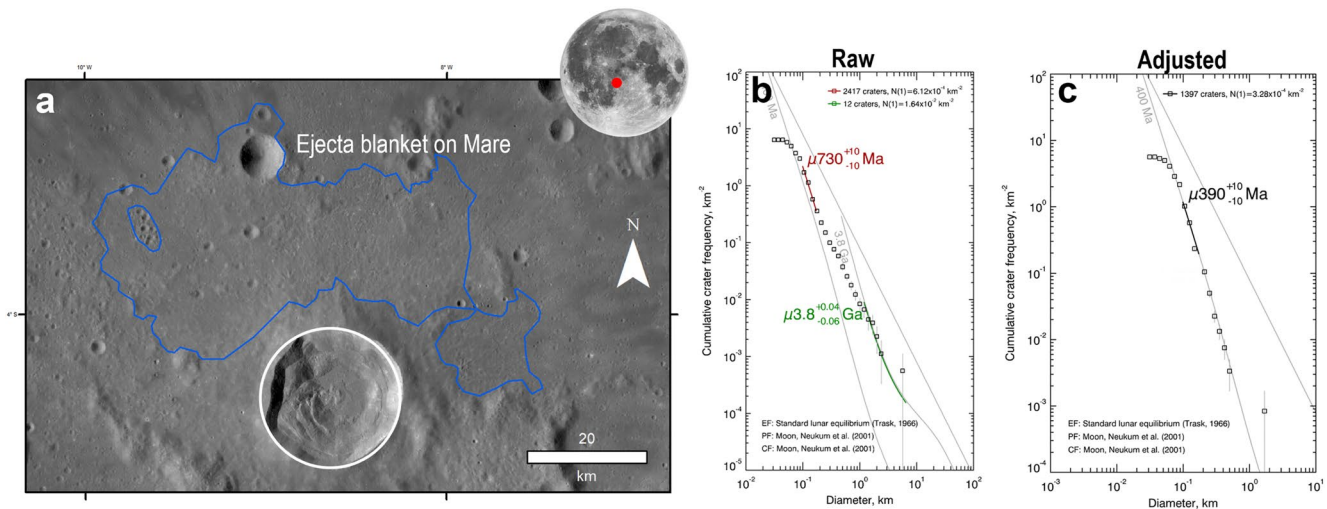
**Figure 5.** (a) Xu et al. (2022)'s Lalande 'ejecta blanket on mare' count area of Lalande crater (blue polygons, 1,780 km²) on Kaguya Terrain Camera tiles; (b) CSFD and model age isochrons for the 'ejecta blanket on mare' count area using 2,417 detections ranging between 100 and 170 m in diameter (red isochron), and 12 detections between 1.2 and 7 km in diameter (green isochron); (c) CSFD and model age isochron using the remaining 1,397 craters ranging between 100 m and 170 km in diameter. The gray 400 Ma isochron plotted on panels b and c corresponds to that reported by Xu et al. (2022) for the 'ejecta blanket on mare' count area. The crater images are presented in a stereographic map projection, with the count area locations (see Table 1) as the projection center point.

count area the same as the published studies (outlined in the Table 2 caption). All CSFDs were binned in the 4th root-2 system, as not all the cited datasets consistently stated the binning method used. All model age errors are a function of the number of craters counted. The margins are calculated using this equation: $\sqrt{n}$, where $n$ is the number of craters in a size bin (Crater analysis techniques working group, 1979). All the crater detections, counting areas, and CraterStats II files are in Data Set S3.

### 3.1. Craters

The NAC and Kaguya CDA models were run over images of within published crater count areas for North Ray (Figure 4a), Lalande (Figure 5a), Tycho (NAC and WAC areas) (Figure 6a) and Copernicus craters (Figure 7a). The raw crater detections within these count areas produced the presented raw CSFDs. Each of the four crater sites resulted in varying differences between the published values and our values. For example, the greatest differences (of 45% and 35%) were observed for Lalande's crater formation age (Figure 5b) and the Tycho NAC count areas (Figures 6c and 6d), respectively. In addition, Lalande's underlying mare unit age was also derived from the successful detection of large impact craters (see Figure 5b)—this model age was also calculated and reported by Xu et al. (2022) in their analysis of the crater. Conversely, this is where we found the lowest age difference, where the CDA and published values are identical (Figure 11c).

In order to better understand the effects of secondary and "pre-existing" crater contamination within all impact crater count areas, we tried to remove all contaminants from the datasets. Based on their relative spatial distribution of the crater directions, areas determined to be secondary crater clusters and craters flagged as "pre-existing" were mapped and subtracted from all the count areas. This was done for North Ray (Figure 6c), Tycho WAC (Figure 6b), and Copernicus craters (Figure 7c). The count areas for Lalande and Tycho NAC were not adjusted, as no significant secondary crater clusters were mapped. Though, flagged "pre-existing" craters were removed from the Lalande crater data set. The area files and crater detections are located in Data Sets S2 and S3.

New CFSDs were plotted for each site from the adjusted data, and isochrons were drawn using the same fit ranges as before (Figure 4d, 5c, 6e, 7d). Across the four sites, three sites (North Ray, Lalande, and Copernicus) showed minimal differences (<20%) between the adjusted and published values (Figure 11f). The greatest differences (>30%) were observed for both Tycho WAC and NAC count areas (Figure 11f). All the results for each crater site are better summarized and displayed in Table 3 and Figure 11.
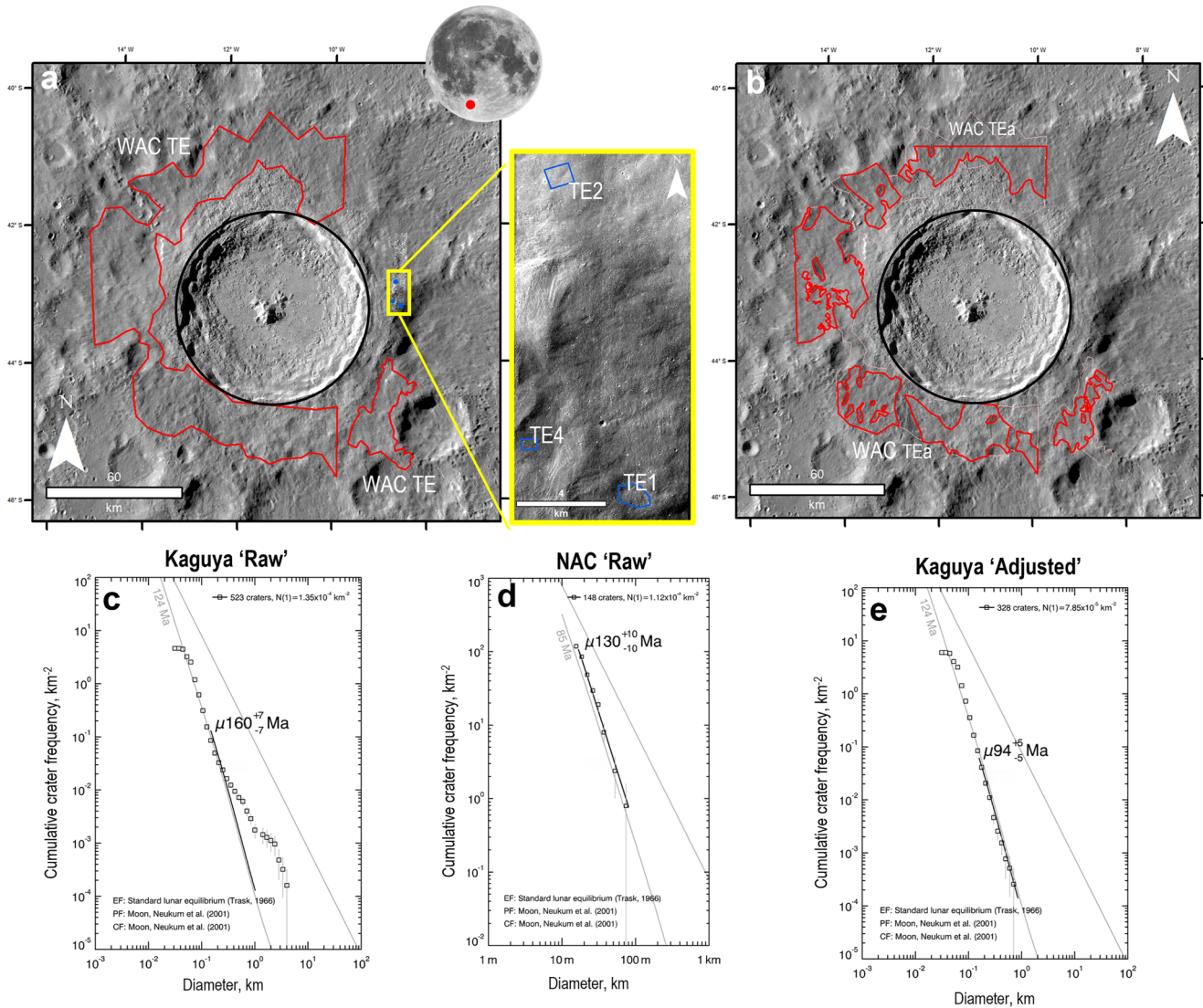
**Figure 6.** (a) Hiesinger et al. (2012)'s WAC TE (red polygons, 6710 km²) and NAC TE1,2,4 count areas (blue polygons, 0.407 km²) for Tycho crater ejecta on Kaguya image tiles and NAC image pair M104570590R/L; (b) adjusted Tycho count areas WAC TEa (red polygons, 3980 km²) and NAC TEa areas (blue polygons, 9.09 km²) on Kaguya image tiles and NAC image pair M104570590R/L; (c) CSFD and model age isochron for the WAC TE areas over the Kaguya image tile detections using 523 craters between 200 m and 1 km in diameter (Note that this CSFD shows an obvious representation of large craters (>500 m) overlaid by the ejecta, implying that Hiesinger et al. (2012) discarded most of these craters in their counting); (d) CSFD and model age isochron for areas TE1, 2 and 4 using 504 NAC detections between 20 and 100 m in diameter; (e) CSFD and model age isochron for the adjusted WAC TEa areas over the Kaguya image tiles, using 328 craters between 200 m and 1 km in diameter. The gray 124 Ma and 85 Ma isochron plotted on panels c, d and e correspond to the model age Hiesinger et al. (2012) reported for the WAC and NAC count areas. The crater images are presented in a stereographic map projection, with the count area locations (see Table 1) as the projection center point.

### 3.2. Mare

The same age derivation processes were conducted over the four mare sites, where only the Kaguya CDA model was applied on Kaguya images. The raw crater detections within published count areas (Table 2) for Chang'E-5 area #21 and #05 (Figures 8a and 8c), as well as units P60 (Figure 9a) and I30 (Figure 10a) were plotted as CSFDs. Isochrons were drawn, and the raw model ages and N(1) values were calculated for each site (Figures 8–10). Three of the four mare sites showed considerably older ages and higher N(1) values when compared to the values reported by Giguere et al. (2022) and Hiesinger et al. (2000, 2011) and Hiesinger (2003). This difference ranged from 20% to 45%, with CE-5 site #05 showing the lowest difference and areas P60 and I30 collectively showing the highest (Figure 11c). Chang'E-5 site #21 (i.e., the CE-5 land site) was of particular interest, as this showed the lowest difference of all sites analyzed within this study, at 10% (Figure 11c). The significance of the Chang'E-5 results will be discussed in a later section.
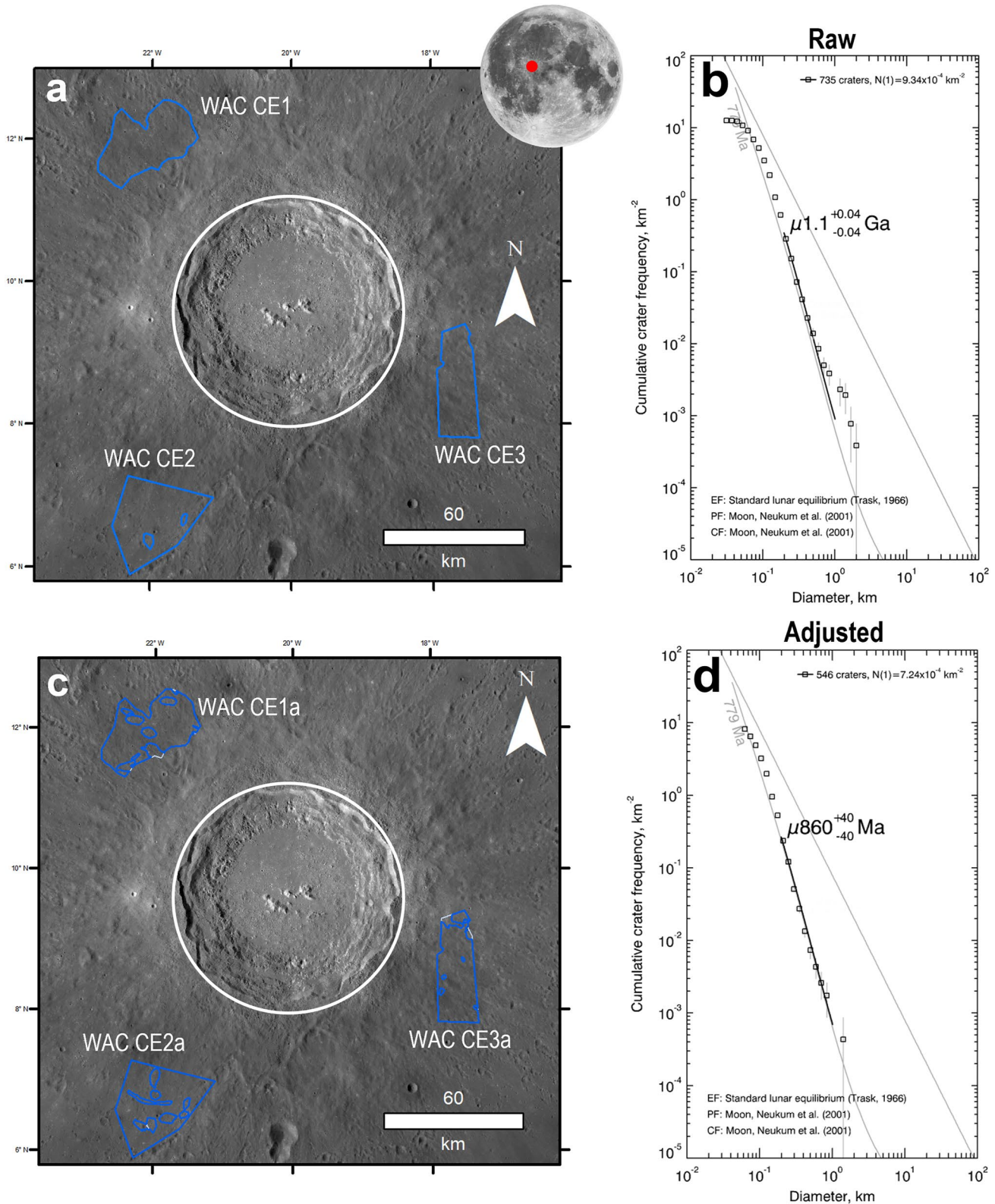
**Figure 7.** (a) Hiesinger et al. (2012)'s Copernicus WAC CE1-3 count areas (blue polygons, 2630 km²); (b) CSFD and model age isochron for areas WAC CE1-3 using 735 craters between 200 m and 1 km in diameter; (c) this study's adjusted WAC CE1a-3a count areas (blue polygon, 2305 km²); (d) adjusted CSFD and model age isochron for areas WAC CE1a-3a using the remaining 546 craters between 200 m and 1 km in diameter. The gray 779 Ma isochron plotted on panels (b and d), refers to the model age reported by Hiesinger et al. (2012) for the WAC CE1-3 count areas. The crater images are presented in a stereographic map projection, with the count area locations (see Table 1) as the projection center point.

**Table 3**
*Summary of Our Raw and Adjusted Results for Each Counting Area; Including Location, Area ID, Image Data, Area Size, $N_{cum}(1)$ [per $km^2$], and Model Ages (With Errors)*

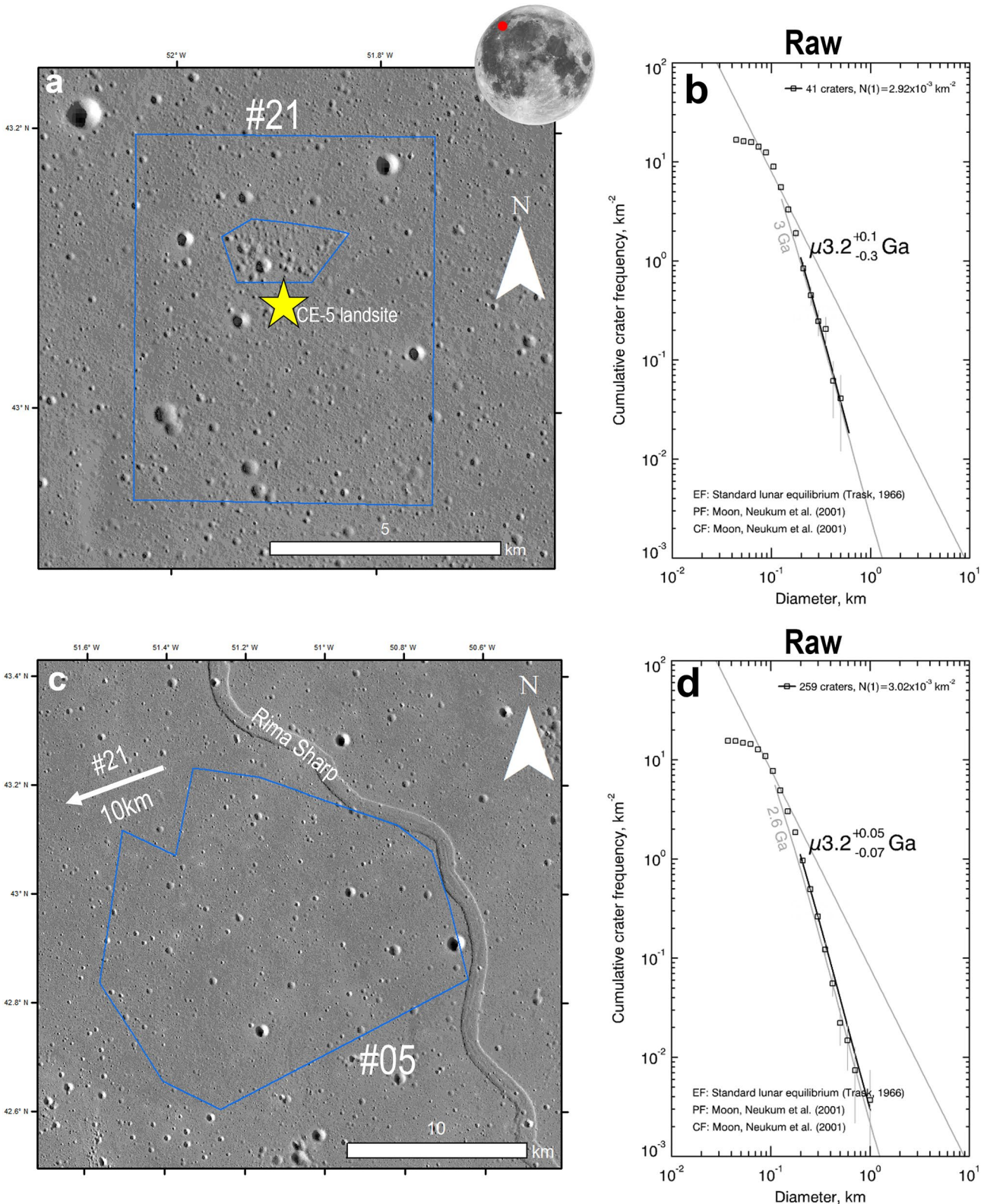| Location | Image data | Count area | Fit range | Raw | | | | | Adjusted | | | | |
|---|---|---|---|---|---|---|---|---|---|---|---|---|---|
| | | | | Area (km²) | Craters fitted | $N_{cum}(1)$ | Model age (Ma) | Error (Ma) | Area (km²) | Craters fitted | $N_{cum}(1)$ | Model age (Ma) | Error (Ma) |
| North Ray | NAC | NR1-4 | 20–100 m | 2.12 | 137 | 6.03E−05 | 72 | 6 / −6 | 0.86 | 48 | 4.69E−05 | 56 | 8 / −8 |
| Lalande | Kaguya TC | Ejecta blanket on Mare | 100–170 m | 1,780 | 2,417 | 6.12E−04 | 730 | 10 / −10 | / | 1,397 | 3.27E−04 | 390 | 10 / −10 |
| | | | >1.2 km | | 12 | 1.81E−02 | 3,800 | 40 / −60 | | / | / | / | / |
| Tycho | NAC | TE | 20–100 m | 0.41 | 148 | 1.09E−04 | 130 | 10 / −10 | / | / | / | / | / |
| | Kaguya TC | WAC TE | 150 m–1 km | 6,710 | 523 | 1.34E−04 | 160 | 7 / −7 | 3,980 | 328 | 7.88E−05 | 94 | 5 / −5 |
| Copernicus | Kaguya TC | WAC CE1-3 | 200 m–1 km | 2,630 | 735 | 9.22E−04 | 1,100 | 40 / −40 | 2,305 | 546 | 7.21E−04 | 860 | 40 / −40 |
| Chang'E-5 | Kaguya TC | #21 | 200–600 m | 48 | 41 | 2.91E−03 | 3,200 | 100 / −300 | / | / | / | / | / |
| | | #05 | 250 m–1 km | 272 | 259 | 3.23E−03 | 3300 | 50 / −70 | / | / | / | / | / |
| Oceanus Procellarum | Kaguya TC | P60 | >400 m | 1,930 | 73 | 1.84E−03 | 2,200 | 300 / −300 | 1,210 | 39 | 1.17E−03 | 1,400 | 200 / −200 |
| Mare Imbrian | Kaguya TC | 130 | >400 m | 3,108 | 299 | 3.23E−03 | 3,300 | 40 / −40 | 2,450 | 130 | 1.93E−03 | 2,300 | 200 / −200 |

**Figure 8.** (a) Giguere et al. (2022)'s count area #21 of the Chang'E-5 (blue polygon, 48 km²) on a Kaguya tile, the yellow star is the Chang'E-5 lander landing site (43.05°N 51.91°W); (b) CSFD and model age isochron of area #21 using Kaguya 41 detections between 200 and 600 m in diameter; (c) Giguere et al. (2022)'s count area #05 (blue polygon, 270 km²) on a Kaguya image tile; (d) CSFD and model age isochron of area #05 using 259 craters between 200 m and 1 km in diameter. The gray 3.0 Ga and 2.6 Ga isochrons plotted on panels (b and d) correspond to the model age Giguere et al. (2022) reported for count areas #21 and #05, respectively. The crater images are presented in a stereographic map projection, with the count area locations (see Table 1) as the projection center point.
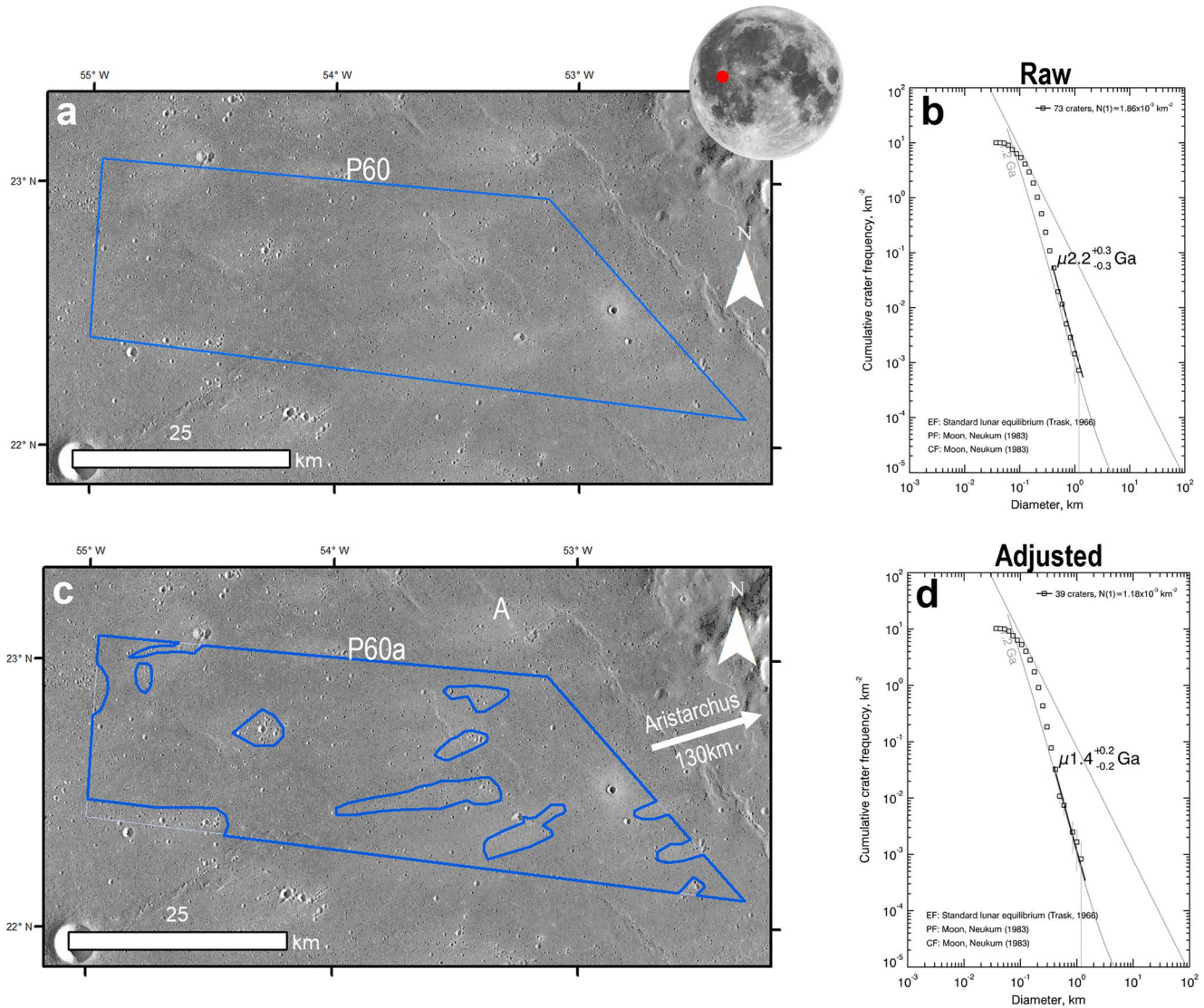
**Figure 9.** (a) Hiesinger (2003) count area for unit P60 (blue polygon, 1930 km²) on Kaguya image tiles; (b) CSFD and model age isochron for P60 using 73 craters between 400 m and 1.7 km in diameter; (c) this study's adjusted count area of unit P60a (blue polygons, 1,210 km²) on Kaguya image tiles; (d) adjusted CSFD and model isochron for area P60a, using 39 craters between 400 m and 1.7 km in diameter. The gray 1.2 Ga isochron plotted on panels b and d corresponds to that of Hiesinger (2003)'s reported for the P60 count area. The crater images are presented in a stereographic map projection, with the count area locations (see Table 1) as the projection center point.

Secondary crater clusters that could contaminate the crater count data sets were investigated across each mare site. However, we did not conduct a 'pre-existing' crater analysis, as thick continuous impact ejecta does not overlay these sites. Furthermore, we did not adjust Giguere et al. (2022)'s count area #21 and #05 for Chang'E-5 (Figures 8b and 8d), as the authors already investigated and removed secondary craters to a sufficient level. However, for the unit P60 and I30 count areas, we did map a significant amount of secondary crater clusters cutting across the count areas, likely deposited from the nearby Aristarchus and Copernicus impacts (Figures 9c and 10c). The adjusted data set model ages and N(1) values for these sites showed minimal differences (<20%) when compared against the published ages (Figure 11f). All the results for each mare site are better summarized and displayed in Table 3 and Figure 11.
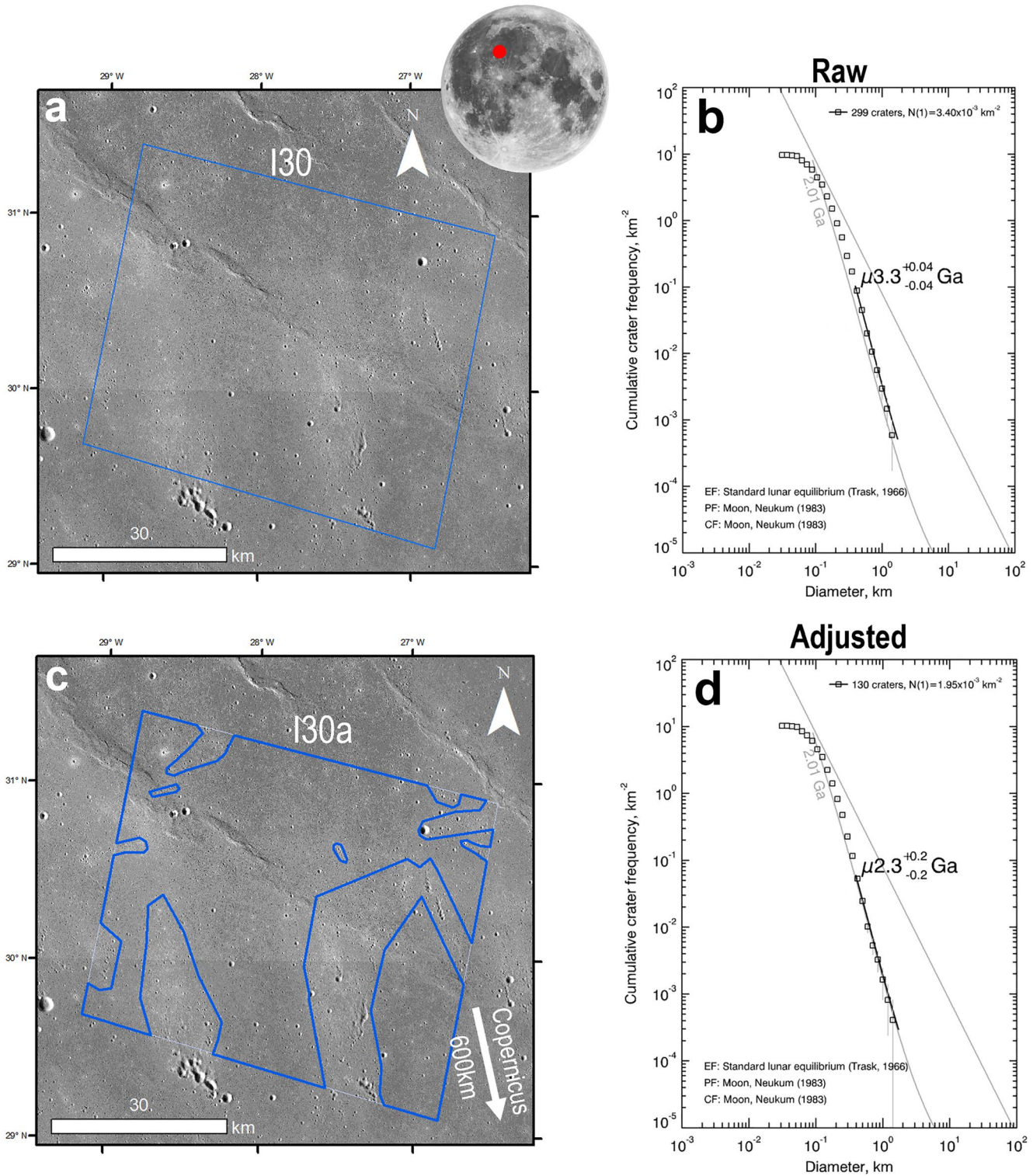
**Figure 10.** (a) Hiesinger et al. (2000) count area for unit I30 (blue polygon, 3108 km²) on Kaguya image tiles; (b) CSFD and model age isochron for I30 using 299 craters between 400 m and 1.5 km in diameter; (c) this study's adjusted count area of unit I30a (blue polygons, 2,450 km²) on Kaguya image tiles; (d) adjusted CSFD and model isochron for area I30a, using 130 craters between 400 m and 1.5 km in diameter. The gray 2.01 Ga isochron plotted on panels b and d corresponds to that Hiesinger et al. (2000) reported for the I30 count area. The crater images are presented in a stereographic map projection, with the count area locations (see Table 1) as the projection center point.
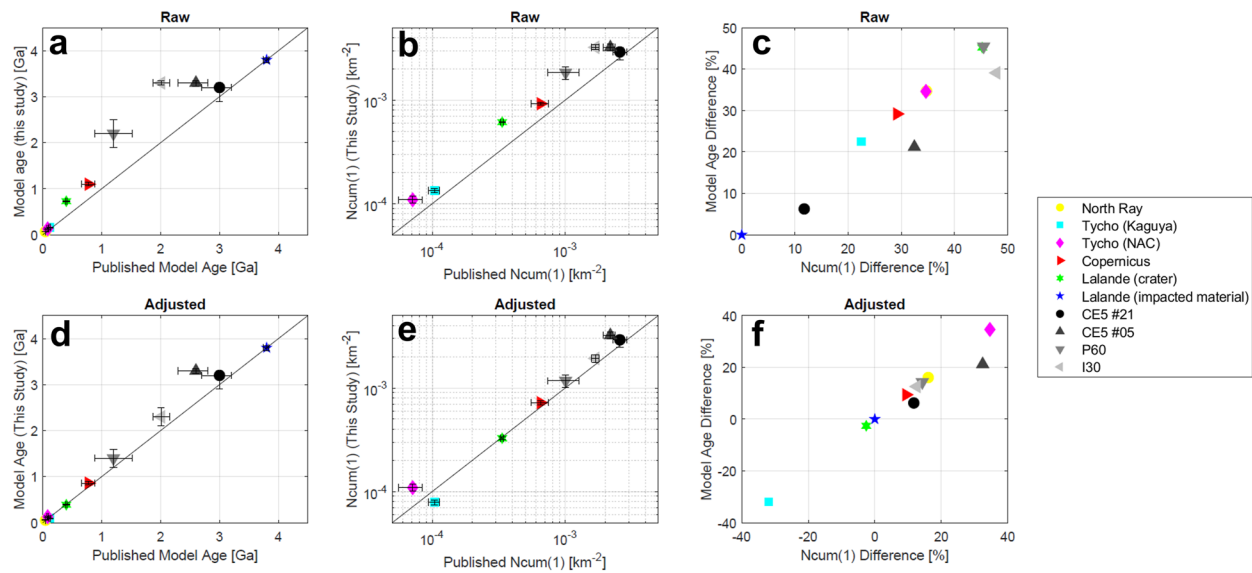
**Figure 11.** Summary of the comparison of the results for the 9 analyzed count areas. (a) Raw model ages calculated in this study against the published model ages for each count area; (b) Raw N(1) densities from this study against the published N(1) densities for each count area; (c) The percent differences between the Raw and published model ages and cratering densities for each count area; (d) adjusted model ages calculated in this study against the published model ages for each count area; and (e) adjusted N(1) densities from this study against the published N(1) densities for each count area. (f) The percentage differences between the adjusted and published model ages and N(1) densities for each count area. The diagonal black lines in panel a, b, d, and e show the linear relationship between this study and the published data (i.e., the closer the data plots are to the line, the more similar they are).

## 4. Discussion

### 4.1. The CDAs Performance in Model Age Derivations

The CDA performed adequately, as shown by the validation metrics (Recall, Precision and F1 values) in the presented evaluations (see Text S2 in Supporting Information S1) and efficiently detected craters across all the studied sites (Figure 2). While only looking at the raw detection data across all the studied count areas, there was a regular overestimation in the N(1) values and model ages when compared to the published values. This overestimation ranged from 10% to 45% (Figure 11c). As stated above, the evaluation of the detection model trained on Kaguya TC images shows similar performance to human mapping (diameter estimation (see Figure S2 in Supporting Information S1), Recall, and Precision (see Table S1 in Supporting Information S1)). The increased model age and crater density can be attributed to secondary crater clusters and "pre-existing" craters included within the raw count data set for the CSFDs. These raw CSFD results emphasize that it is up to the researcher to make final decisions on which counted craters represent the geological surface they wish to date, and not blindly rely on automated crater detections. We argue that for automated crater datasets to be used properly for crater counting, the researcher must undertake a process of due diligence and geologic reasoning before using the results. In this analysis, we examined and adjusted the count areas and crater data set.

The adjustment of the crater datasets for each site (i.e., secondary and "pre-existing" craters removal and reduction of the count areas) results in younger model ages and CSFDs more comparable with manual counts (Figure 11f). Overall, the N(1) values and the subsequent ages for 6 out of the 9 count areas range from −3% to +18%, with some outliers (Figure 11f). It is reasonable to attribute a systematic difference to an automated technique, but this could also reflect researcher crater detection variability (Robbins et al., 2014), or the differences between image datasets (Giguere et al., 2022). We argue that the reduction in model ages could be attributed to the reduction of the count areas which can introduce a non-random pattern in the cratering record. This could lead to the exclusion of larger primary craters that survived the obliteration processes (Warner et al., 2015). Moreover, the reduction could also reflect the successful removal of secondary craters clusters, lowering the relative N(1) values. Though, the small differences (<20%) between the adjusted and published model ages, for 6 out of the 9 count areas (Figure 11f), reflect an acceptable reproducibility of the manual crater count findings. The discrepancies regarding the Tycho areas (WAC TE and NAC TE) and the Chang'E-5 #05 will be discussed in the following subsection, where we look at some possible reasons for the differences.

### 4.1.1. The Tycho Crater Ages

The results obtained on the adjusted Tycho WAC count area on the Kaguya TC image tiles (Figure 6e) were significantly different compared to the values reported by Hiesinger et al. (2012) and the other values reported within this study. The WAC TE count area was the only site that displayed an underestimation in the cratering density and model age values (Figure 11f). An underestimation would reflect that our CDA significantly did not detect as many craters compared to the base study, but we argue this was not an error. For the Tycho crater data set, no craters within the count area were flagged as 'pre-existing'; therefore, no degraded craters were outright removed. Therefore, the observed underestimation of crater density could be attributed to the inclusion of additional, or interpreted (see Figure S3 in Supporting Information S1), craters by Hiesinger et al. (2012) in their data set, or the removal of additional secondary crater clusters that Hiesinger et al. (2012) did not identify. We argue that it may have been portions of both. The base study reported craters down to ∼100 m in diameter and derived an age using an isochron fitted between ∼150 m and 1 km. This fit range is substantially below the 10-pixel accuracy/reliability cut-off now recommended for crater counting (Robbins et al., 2014; Wang et al., 2020). Therefore, the crater data set can include other circular structures, such as large boulders (100–200 m), which are very difficult to resolve at the WAC resolution scale (100 m/px) (see Figure S3 in Supporting Information S1). This will lead to an overestimation of the base crater density and, thus, to the lower crater density we measured.

Conversely, the CSFD we extracted on the adjusted NAC Tycho TE count areas led to an overestimation of the crater density and model age by the highest amount at +30% (Figure 11f). Based on a check of the CDA performance, and a visual inspection of the craters detected in these areas, this discrepancy likely originates from a difference in identifying primary and secondary craters between our study and Hiesinger et al. (2012)'s mapping.

Furthermore, the defined NAC count areas have complex lighting conditions across the count areas (see, Figure S5 in Supporting Information S1), where crater identification can significantly differ between those NAC count areas leading to fewer (or more) identified craters (Giguere et al., 2022). Additionally, we excluded a count area (NAC TE3), due to location on the crater rim slope with less non-ideal lighting conditions (incidence angle of ∼42°). This will affect the model age, but we could not reconstruct the published NAC TE CSFDs, as there is no supplied list of Hiesinger et al. (2012)'s crater datasets. Therefore, it is not possible to reconstruct all the counts to determine regions where the crater counting was significantly different or if potential mapping variability or errors were made (on both sides).

Following this notion, both values (published and CDA) for the Tycho count areas are realistic when placed in the scope of other crater count analyses (though conducted on different geographical areas with different production functions using different methods). For example, using thermophysical characteristics of lunar impact ejecta, Mazrouei et al. (2019) report a significantly different model age of 85 Ma. Whereas using crater counts on the proximal ejecta blanket with the Neukum (1984) functions, Terada et al. (2020) derived a model age of 58 Ma. Placing all values in the scope of other studies, the result of our semi-automatic model age derivation technique falls within a realistic range of reported values for the formation age of Tycho crater.

### 4.1.2. The Chang'E-5 Site Ages

The count areas, Chang'E-5 #21 and #05, which were not adjusted in this study, show a model age overestimation that ranges from 10% to ∼20% (Figure 11c), respectively. The crater density N(1) of area #21 is well within what the manual crater identification variability between experts could lead at this mapping scale on mare areas (±∼20%, Robbins et al., 2014), whereas area #05 had the second greatest N(1) difference observed at +32%. We also note that our derived N(1) values for these sites, with a distance of only of ∼15 km between each other, were very similar (area #21, $2.91 \times 10^{-3}$ km$^{-2}$; area #05, $3.23 \times 10^{-3}$ km$^{-2}$), whereas Giguere et al. (2022)'s crater densities differ by ∼17%. The crater density we report is almost twice as high as those measured in previous studies aiming to extract the CSFD around the Chang'E-5 LS (area #21), mainly for the purpose of the lunar chronology recalibration (Jia et al., 2020; Qian et al., 2021; Wu et al., 2018). Although this is out of the scope of this study, the variability in crater densities measured in this area will be worth investigating in future studies. Mare site #05 was further investigated, and a significant difference in total craters counted was found between Giguere et al. (2022) and our CDA (Figure 12). Most count differences were restricted to craters between 200 and 400 m, where the CDA detected over twice as many craters (Table S3 in Supporting Information S1), of which most were moderately degraded. Giguere et al. (2022) discussed the influence of lighting conditions and image quality on the resulting crater measurements
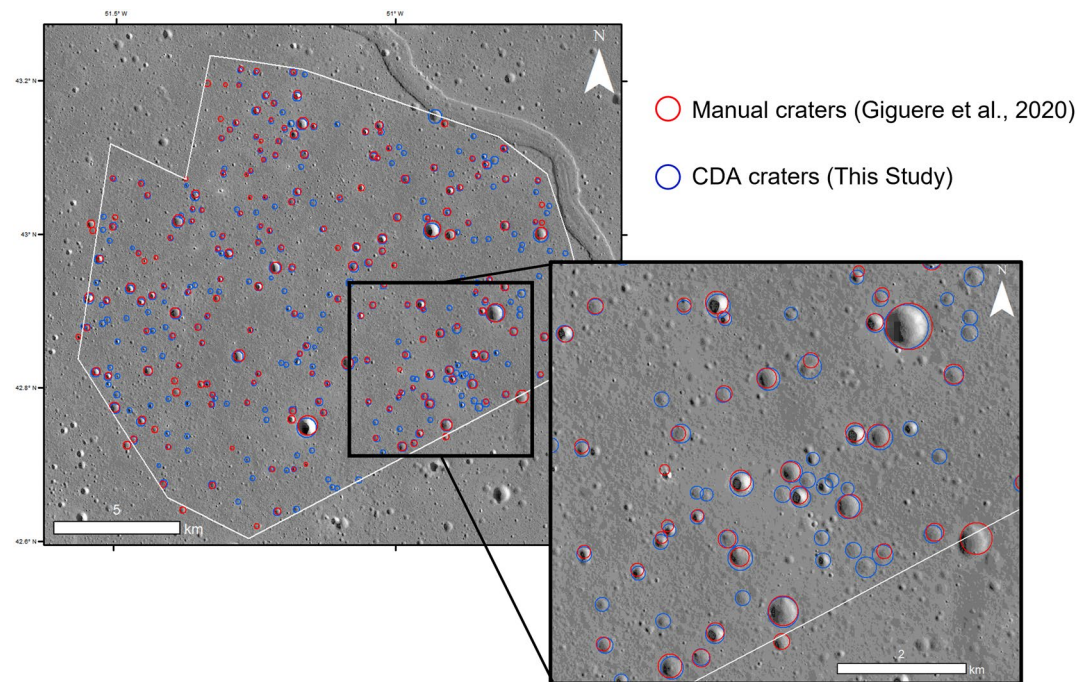
**Figure 12.** Total crater counts ≥200 m in diameter over Giguere et al. (2022)'s Chang'E-5 #05 count area. The white polygon denotes the #05 count area boundary, red circles represent 178 craters measured by Giguere et al. (2022), the blue circles represent the 314 craters detected by the CDA (Table S3 in Supporting Information S1).

and argued that this ingrains inconsistencies between researchers. Where Giguere et al. (2022) used a series of NAC images with different lighting conditions, we used a single Kaguya TC tile with consistent lighting across the area. It is most likely that this effect resulted in the different crater rim measurements and crater identification.

## 5. Conclusion

This study compares and assesses the viability of using model ages and crater densities derived from an automatic detection method using a Crater Detection Algorithm (CDA). We compare our values to current published manual counts for nine different lunar crater count areas distributed over the lunar near-side. The results show that using a CDA trained on Lunar Reconnaissance Orbiter - Narrow Angle Camera (LRO-NAC) and Kaguya TC (Kaguya TC) images is a viable and timely approach for detecting small craters on young lunar surfaces. The results of the study show that the use of a CDA can be an effective tool in deriving model ages and crater densities with an acceptable level of reproducibility concurrent with human mapping. When un-adjusted, the results of the CDA can lead to an overestimation of crater density by up to ∼50%. However, with sufficient semi-automated processing to adjust the population and the removal of regions with secondary clusters or "pre-existing" craters, the derived model ages and crater densities were consistent with their published values. Though, the derived model ages and crater densities significantly differed from the published values for two areas, Tycho's ejecta and the Chang'E-5 #05 area. After careful examination, the differences were determined to be mostly due to the differences in image quality, resolution, and researcher variability, which led to inconsistent crater identification. In this respect, this study demonstrates the potential for a CDA for the analysis of numerous lunar sites to derive model ages on a global scale. This use, however, must be in addition to the careful checking of the detections and semi-automatic approaches to remove potential secondary and underlying craters contamination, along with careful geological mapping and interpretations. The CDA could be used to provide valuable information on the recent events that shaped the surface of the Moon and can lead to a better understanding of its recent geological history.

## Data Availability Statement

The Supporting Information S1 is all available in an online repository (https://doi.org/10.5281/zenodo.8045606). The code required to reproduce our algorithm is located on the Yolov5-ultralytics GitHub (https://github.com/ultralytics/yolov5). The CraterStats II Software can be downloaded Freie Universität Berlin software portal (https://

www.geo.fu-berlin.de/en/geol/fachrichtungen/planet/software/_content/software/craterstats.html). The CSFDs for each count area are available in Data Set S3. The Lunar Reconnaissance Orbiter Narrow-Angle Camera (LRO-NAC) images were downloaded from the LROC website (http://wms.lroc.asu.edu/lroc/search). The Isbell et al. (2014) Kaguya TC tiles (both morning and evening) are available at the Kaguya Data Archive (https://darts.isas.jaxa.jp/planet/pdap/selene/).

## References

Ali-Dib, M., Menou, K., Jackson, A. P., Zhu, C., & Hammond, N. (2020). Automated crater shape retrieval using weakly-supervised deep learning. *Icarus*, *345*, 113749. https://doi.org/10.1016/j.icarus.2020.113749

Baldwin, R. B. (1964). Lunar crater counts. *The Astronomical Journal*, *69*, 377. https://doi.org/10.1086/109289

Benedix, G. K., Lagain, A., Chai, K., Meka, S., Anderson, S., Norman, C., et al. (2020). Deriving surface ages on Mars using automated crater counting. *Earth and Space Science*, *7*(3). https://doi.org/10.1029/2019EA001005

Bogard, D. D., Garrison, D. H., McKay, D. S., & Wentworth, S. J. (1992). The age of Copernicus: New evidence for 800+15 million years. *23*, 133.

Cadogan, P. H. (2020). Automated precision counting of very small craters at lunar landing sites. *Icarus*, *348*, 113822. https://doi.org/10.1016/j.icarus.2020.113822

Che, X., Nemchin, A., Liu, D., Long, T., Wang, C., Norman, M. D., et al. (2021). Age and composition of young basalts on the Moon, measured from samples returned by Chang'E-5. *Science*, *374*(6569), 887–890. https://doi.org/10.1126/science.abl7957

Craddock, R. A., & Howard, A. D. (2000). Simulated degradation of lunar impact craters and a new method for age dating farside mare deposits. *Journal of Geophysical Research*, *105*(E8), 20387–20401. https://doi.org/10.1029/1999JE001099

Crater analysis techniques working group. (1979). Standard techniques for presentation and analysis of crater size-frequency data. *Icarus*, *37*(2), 467–474. https://doi.org/10.1016/0019-1035(79)90009-5

DeLatte, D. M., Crites, S. T., Guttenberg, N., & Yairi, T. (2019). Automated crater detection algorithms from a machine learning perspective in the convolutional neural network era. *Advances in Space Research*, *64*(8), 1615–1628. https://doi.org/10.1016/j.asr.2019.07.017

Drozd, R. J., Hohenberg, C. M., Morgan, C. J., Podosek, F. A., & Wroge, M. L. (1977). Cosmic ray exposure history at Taurus-Littrow (Vol. *8*, p. 254).

Drozd, R. J., Hohenberg, C. M., Morgan, C. J., & Ralston, C. E. (1974). Cosmic-ray exposure history at the Apollo 16 and other lunar sites: Lunar surface dynamics. *Geochimica et Cosmochimica Acta*, *38*(10), 1625–1642. https://doi.org/10.1016/0016-7037(74)90178-1

Dundas, C. M., & McEwen, A. S. (2007). Rays and secondary craters of Tycho. *Icarus*, *186*(1), 31–40. https://doi.org/10.1016/j.icarus.2006.08.011

Fairweather, J. H., Lagain, A., Servis, K., Benedix, G. K., Kumar, S. S., & Bland, P. A. (2022). Automatic mapping of small lunar impact craters using LRO-NAC images. *Earth and Space Science*, *9*(7). https://doi.org/10.1029/2021EA002177

Fassett, C. I. (2016). Analysis of impact crater populations and the geochronology of planetary surfaces in the inner solar system: Crater Populations and Surface Chronology. *Journal of Geophysical Research: Planets*, *121*(10), 1900–1926. https://doi.org/10.1002/2016JE005094

Fassett, C. I., & Thomson, B. J. (2014). Crater degradation on the lunar Maria: Topographic diffusion and the rate of erosion on the Moon: Crater degradation on the lunar Maria. *Journal of Geophysical Research: Planets*, *119*(10), 2255–2271. https://doi.org/10.1002/2014JE004698

Fortezzo, C. M., Spudis, P. D., & Harrel, S. L. (2020). Release of the digital unified global geologic map of the Moon at 1:5,000,000-scale. 2760.

Giguere, T. A., Boyce, J. M., Gillis-Davis, J. J., Trang, D., & Stopar, J. D. (2022). Lava flow ages in northeastern Oceanus Procellarum: The need for calibrating crater counting procedures. *Icarus*, *375*, 114838. https://doi.org/10.1016/j.icarus.2021.114838

Haruyama, J., Ohtake, M., Matsunaga, T., Morota, T., Yokota, Y., Honda, C., et al. (2008). Planned radiometrically calibrated and geometrically corrected products of lunar high-resolution Terrain Camera on SELENE. *Advances in Space Research*, *42*(2), 310–316. https://doi.org/10.1016/j.asr.2007.04.062

Hiesinger, H. (2003). Ages and stratigraphy of mare basalts in Oceanus Procellarum, mare Nubium, mare Cognitum, and mare Insularum. *Journal of Geophysical Research*, *108*(E7), 5065. https://doi.org/10.1029/2002JE001985

Hiesinger, H., Head, J. W., Wolf, U., Jaumann, R., & Neukum, G. (2011). Ages and stratigraphy of lunar mare basalts: A synthesis. In W. A. Ambrose & D. A. Williams (Eds.), *Recent advances and current research issues in lunar stratigraphy*. Geological Society of America. https://doi.org/10.1130/2011.2477(01

Hiesinger, H., Jaumann, R., Neukum, G., & Head, J. W. (2000). Ages of mare basalts on the lunar nearside. *Journal of Geophysical Research*, *105*(E12), 29239–29275. https://doi.org/10.1029/2000JE001244

Hiesinger, H., van der Bogert, C. H., Pasckert, J. H., Funcke, L., Giacomini, L., Ostrach, L. R., & Robinson, M. S. (2012). How old are young lunar craters? *Journal of Geophysical Research*, *117*(E12), E00H10. https://doi.org/10.1029/2011JE003935

Hildebrand, A. R., Pilkington, M., Ortiz-Aleman, C., Chavez, R. E., Urrutia-Fucugauchi, J., Connors, M., et al. (1998). Mapping Chicxulub crater structure with gravity and seismic reflection data. *Geological Society, London, Special Publications*, *140*(1), 155–176. https://doi.org/10.1144/GSL.SP.1998.140.01.12

Isbell, C., Gaddis, L., Garcia, P., Hare, T., & Bailen, M. (2014). Kaguya terrain camera mosaics. #2268.

Jia, M., Yue, Z., Di, K., Liu, B., Liu, J., & Michael, G. (2020). A catalogue of impact craters larger than 200 m and surface age analysis in the Chang'E-5 landing area. *Earth and Planetary Science Letters*, *541*, 116272. https://doi.org/10.1016/j.epsl.2020.116272

Jocher, G. (2022). *Ultralytics YOLOv5. (Python)*. GitHub. Retrieved from https://github.com/ultralytics/yolov5

Kirchoff, M. R., Marchi, S., Bottke, W. F., Chapman, C. R., & Enke, B. (2021). Suggestion that recent (≤3 Ga) flux of kilometer and larger impactors in the Earth-Moon system has not been constant. *Icarus*, *355*, 114110. https://doi.org/10.1016/j.icarus.2020.114110

Lagain, A., Benedix, G. K., Servis, K., Baratoux, D., Doucet, L. S., Rajšic, A., et al. (2021). The Tharsis mantle source of depleted shergottites revealed by 90 million impact craters. *Nature Communications*, *12*(1), 6352. https://doi.org/10.1038/s41467-021-26648-3

Lagain, A., Bouley, S., Baratoux, D., Costard, F., & Wieczorek, M. (2020). Impact cratering rate consistency test from ages of layered ejecta on Mars. *Planetary and Space Science*, *180*, 104755. https://doi.org/10.1016/j.pss.2019.104755

Lagain, A., Bouley, S., Zanda, B., Miljković, K., Rajšić, A., Baratoux, D., et al. (2022). Early crustal processes revealed by the ejection site of the oldest Martian meteorite. *Nature Communications*, *13*(1), 3782. https://doi.org/10.1038/s41467-022-31444-8

Lagain, A., Kreslavsky, M. A., Baratoux, D., Liu, Y., Devillepoix, H. A. R., Bland, P. A., et al. (2022). Has the impact flux of small and large asteroids varied through time on Mars, the Earth and the Moon? *Earth and Planetary Science Letters*, *579*, 117362. https://doi.org/10.1016/j.epsl.2021.117362

Lagain, A., Servis, K., Benedix, G. K., Norman, C., Anderson, S., & Bland, P. A. (2021). Model age derivation of large Martian impact craters, using automatic crater counting methods. *Earth and Space Science*, *8*(2). https://doi.org/10.1029/2020EA001598

Li, H.-C., Zhang, N., Yue, Z.-Y., & Zhang, Y.-Z. (2021). Lunar cratering asymmetries with high lunar orbital obliquity and inclination of the Moon. *Research in Astronomy and Astrophysics*, *21*(6), 140. https://doi.org/10.1088/1674-4527/21/6/140

Mazrouei, S., Ghent, R. R., Bottke, W. F., Parker, A. H., & Gernon, T. M. (2019). Earth and Moon impact flux increased at the end of the Paleozoic. *Science*, *363*(6424), 253–257. https://doi.org/10.1126/science.aar4058

Melosh, H. J. (1989). *Impact cratering: A geologic process*. Oxford University Press. Retrieved from https://books.google.com.au/books?id=nZwRAQAAIAAJ

Michael, G. G., & Neukum, G. (2010). Planetary surface dating from crater size–frequency distribution measurements: Partial resurfacing events and statistical age uncertainty. *Earth and Planetary Science Letters*, *294*(3–4), 223–229. https://doi.org/10.1016/j.epsl.2009.12.041

Neukum, G. (1984). *Meteoritenbombardement und Datierung planetarer Oberflachen (Meteorite bombardment and dating of planetary surfaces)*. University of Munich.

Neukum, G., Ivanov, B. A., & Hartmann, W. K. (2001). Cratering records in the inner solar system in relation to the lunar reference system. In R. Kallenbach, J. Geiss, & W. K. Hartmann (Eds.), *Chronology and evolution of Mars* (Vol. 12, pp. 55–86). Springer Netherlands. https://doi.org/10.1007/978-94-017-1035-0_3

Öpik, E. J. (1960). The lunar surface as an impact counter. *Monthly Notices of the Royal Astronomical Society*, *120*(5), 404–411. https://doi.org/10.1093/mnras/120.5.404

Pawsey (2023). Pawsey supercomputing centre. Retrieved from https://pawsey.org.au/

Pike, R. J. (1974). Ejecta from large craters on the Moon: Comments on the geometric model of McGetchin et al. *Earth and Planetary Science Letters*, *23*(3), 265–271. https://doi.org/10.1016/0012-821X(74)90114-9

Pozzobon, R., Tusberti, F., Pajola, M., & Massironi, M. (2020). Geologic map, landing site selection and Traverse planning in Copernicus crater. https://doi.org/10.5281/ZENODO.5127777

Qian, Y., Xiao, L., Head, J. W., van der Bogert, C. H., Hiesinger, H., & Wilson, L. (2021). Young lunar mare basalts in the Chang'E-5 sample return region, northern Oceanus Procellarum. *Earth and Planetary Science Letters*, *555*, 116702. https://doi.org/10.1016/j.epsl.2020.116702

Redmon, J., Vivvala, S., Girshick, R., & Farhadi, A. (2016). You only look once: Unified, real-time object detection. *Proceedings of the IEEE Conference on Computer Vision and Pattern Recognition (CVPR)*, 779–788.

Robbins, S. J. (2014). New crater calibrations for the lunar crater-age chronology. *Earth and Planetary Science Letters*, *403*, 188–198. https://doi.org/10.1016/j.epsl.2014.06.038

Robbins, S. J., Antonenko, I., Kirchoff, M. R., Chapman, C. R., Fassett, C. I., Herrick, R. R., et al. (2014). The variability of crater identification among expert and community crater analysts. *Icarus*, *234*, 109–131. https://doi.org/10.1016/j.icarus.2014.02.022

Robinson, M. S., Brylow, S. M., Tschimmel, M., Humm, D., Lawrence, S. J., Thomas, P. C., et al. (2010). Lunar reconnaissance orbiter camera (LROC) instrument overview. *Space Science Reviews*, *150*(1–4), 81–124. https://doi.org/10.1007/s11214-010-9634-2

Salamunićcar, G., Lončarić, S., Grumpe, A., & Wöhler, C. (2014). Hybrid method for crater detection based on topography reconstruction from optical images and the new LU78287GT catalogue of lunar impact craters. *Advances in Space Research*, *53*(12), 1783–1797. https://doi.org/10.1016/j.asr.2013.06.024

Sawabe, Y., Matsunaga, T., & Rokugawa, S. (2006). Automated detection and classification of lunar craters using multiple approaches. *Advances in Space Research*, *37*(1), 21–27. https://doi.org/10.1016/j.asr.2005.08.022

Schmitt, H. H., Petro, N. E., Wells, R. A., Robinson, M. S., Weiss, B. P., & Mercer, C. M. (2017). Revisiting the field geology of Taurus–Littrow. *Icarus*, *298*, 2–33. https://doi.org/10.1016/j.icarus.2016.11.042

Sharpton, V. L. (2014). Outcrops on lunar crater rims: Implications for rim construction mechanisms, ejecta volumes and excavation depths: Outcrops constrain crater rim components. *Journal of Geophysical Research: Planets*, *119*(1), 154–168. https://doi.org/10.1002/2013JE004523

Shoemaker, E. M., & Hackman, R. J. (1962). Stratigraphic basis for a lunar time scale. *The Moon*, *14*, 289–300. https://doi.org/10.1017/s007418090017826x

Speyerer, E. J., Robinson, M. S., & Denevi, B. W., & LROC Science Team. (2011). Lunar reconnaissance orbiter camera global morphological map of the Moon. #2387.Update the acknowledgements with.

Stopar, J. D., Robinson, M. S., Barnouin, O. S., McEwen, A. S., Speyerer, E. J., Henriksen, M. R., & Sutton, S. S. (2017). Relative depths of simple craters and the nature of the lunar regolith. *Icarus*, *298*, 34–48. https://doi.org/10.1016/j.icarus.2017.05.022

Terada, K., Morota, T., & Kato, M. (2020). Asteroid shower on the Earth-Moon system immediately before the Cryogenian period revealed by KAGUYA. *Nature Communications*, *11*(1), 3453. https://doi.org/10.1038/s41467-020-17115-6

Trask, N. J. (1966). Size and spatial distribution of craters estimated from the Ranger photographs. Retrieved from https://ntrs.nasa.gov/citations/19660015760

Wang, Y., Xie, M., Xiao, Z., & Cui, J. (2020). The minimum confidence limit for diameters in crater counts. *Icarus*, *341*, 113645. https://doi.org/10.1016/j.icarus.2020.113645

Wang, Y., Zhu, X., & Wu, B. (2019). Automatic detection of individual oil palm trees from UAV images using HOG features and an SVM classifier. *International Journal of Remote Sensing*, *40*(19), 7356–7370. https://doi.org/10.1080/01431161.2018.1513669

Warner, N. H., Gupta, S., Calef, F., Grindrod, P., Boll, N., & Goddard, K. (2015). Minimum effective area for high resolution crater counting of Martian terrains. *Icarus*, *245*, 198–240. https://doi.org/10.1016/j.icarus.2014.09.024

Wilhelms, D. E. (1987). *The geologic history of the Moon (USGS numbered series No. 1348; professional paper, p. 337)*. United States Geological Survey. https://doi.org/10.3133/pp1348

Wu, B., Huang, J., Li, Y., Wang, Y., & Peng, J. (2018). Rock abundance and crater density in the candidate Chang'E-5 landing region on the Moon. *Journal of Geophysical Research: Planets*, *123*(12), 3256–3272. https://doi.org/10.1029/2018JE005820

Xiao, Z., & Strom, R. G. (2012). Problems determining relative and absolute ages using the small crater population. *Icarus*, *220*(1), 254–267. https://doi.org/10.1016/j.icarus.2012.05.012

Xiao, Z., & Werner, S. C. (2015). Size-frequency distribution of crater populations in equilibrium on the Moon. *Journal of Geophysical Research: Planets*, *120*(12), 2277–2292. https://doi.org/10.1002/2015JE004860

Xie, M., & Xiao, Z. (2023). A new chronology from debiased crater densities: Implications for the origin and evolution of lunar impactors. *Earth and Planetary Science Letters*, *602*, 117963. https://doi.org/10.1016/j.epsl.2022.117963

Xie, M., & Zhu, M.-H. (2016). Estimates of primary ejecta and local material for the Orientale basin: Implications for the formation and ballistic sedimentation of multi-ring basins. *Earth and Planetary Science Letters*, *440*, 71–80. https://doi.org/10.1016/j.epsl.2016.02.0122

Xu, L., Qiao, L., Xie, M., & Wu, Y. (2022). Formation age of lunar Lalande crater and its implications for the source region of the KREEP-rich meteorite Sayh al Uhaymir 169. *Icarus*, *386*, 115166. https://doi.org/10.1016/j.icarus.2022.115166

Xu, L., & Xie, M. (2020). Ejecta thickness distribution of the Schrödinger basin on the Moon. *Journal of Geophysical Research: Planets*, *125*(12), e2020JE006506. https://doi.org/10.1029/2020JE006506

Yang, C., Zhao, H., Bruzzone, L., Benediktsson, J. A., Liang, Y., Liu, B., et al. (2020). Lunar impact crater identification and age estimation with Chang'E data by deep and transfer learning. *Nature Communications*, *11*(1), 6358. https://doi.org/10.1038/s41467-020-20215-y

Zanetti, M., Stadermann, A., Jolliff, B., Hiesinger, H., Van Der Bogert, C. H., & Plescia, J. (2017). Evidence for self-secondary cratering of Copernican-age continuous ejecta deposits on the Moon. *Icarus*, *298*, 64–77. https://doi.org/10.1016/j.icarus.2017.01.030

## References From the Supporting Information

Jocher, G. (2021). *Ultralytics YOLOv3. (Python)*. Ultralytics. Retrieved from https://github.com/ultralytics/yolov3

Redmon, J., & Farhadi, A. (2018). YOLOv3: An incremental improvement. ArXiv Preprint ArXivv, Retrieved from https://arxiv.org/abs/1804.02767